DESIGN, SYNTHESIS, AND CHARACTERIZATION OF SUPRAMOLECULAR SELF-ASSEMBLIES FOR MAGNETIC RESONANCE IMAGING

by
Xinpei Mao

A thesis submitted to Johns Hopkins University in conformity with the requirements for the degree of Master of Science in Engineering

Baltimore, Maryland

May, 2016

Abstract

Magnetic resonance imaging (MRI) is one of the most powerful diagnostic modalities for imaging of the brain, cartilage, heart, blood vessels and tumors with superb spatial resolution and soft tissue contrast. However, the commonly used small molecular contrast agents, for example gadolinium complexes, are highly toxic in the free ionic forms and suffer from low MRI sensitivity. Alternatively, nanostructures formed by self-assembling molecules can be employed as carriers for MRI agents, which significantly improves imaging contrast and relatively reduces associated cytotoxicity. Amphiphilic peptides (APs) are rationally designed small molecule peptide conjugates possessing a great potential for self-assembly in aqueous solution. Depending on the design rationale and assembly environment, various one-dimensional morphologies with different physical properties can be obtained upon self-assembly of APs. The inherent biocompatibility of peptidic molecules, combined with their possible bioactivity, renders APs a versatile platform for MRI. Chemical Exchange Saturation Transfer (CEST) is an emerging MRI contrast mechanism, which utilizes special MRI pulses sequence to selectively detect exchangeable protons on each probe at their unique chemical shift, translating them into a frequency-specific molecular imaging agents. In this study, we conjugated Pemetrexed (under the trade name Alimta), the FDA-approved anticancer drug, onto the short peptide sequence, to create an amphiphilic peptide (PemFE) that could form nanofibers hydrogel. Compared with contrast agents labelled with metal chelates, pemetrexed itself has inherent CEST MRI signal at 5.2 ppm frequency offset from the resonance of water. This platform offers us a “label free” method to trace the delivery and distribution of PemFE nanofiber hydrogel in mouse glioma model. Our *in vivo* study demonstrated that the injected PemFE hydrogel in mouse glioma tumors could be detected using CEST MRI for up to 4 days post-implantation.

Advisor: Dr. Honggang Cui **Reader:** Dr. David Gracias

Acknowledgements

First and foremost, I would like to thank my parents, for always giving me unconditional love and support, and encouraging me to study abroad to broaden my horizon and enrich my knowledge. They are my role models, and I would like to thank them for providing me the best life as they can.

What's more, I thank my advisor, Dr. Honggang Cui, who gives me the opportunity to expand my knowledge in his lab. Dr. Cui has been instrumental in shaping my academic career, and educating me to become a better scientist. I really appreciate him for requiring me with the same standard as Ph.D. students, so that I gained so much experience starting from thinking up project ideas to delivering experiments, and finally wrapping up the project as a paper. I would also thank him for the support and reference to my future endeavors.

Then, I would thank Dr. David Gracias for being the reader of my thesis.

Lastly, I would like to thank the former graduate student in Cui lab, Lye Lin Lock. She mentored me as I stepped into the Cui lab, and shared with me all of her knowledge not only from her project but also from her Ph.D. experience.

Table of Contents

List of Figures and Tables

Chapter 1: Introduction

1.1 Basic Principles of Magnetic Resonance Imaging (MRI) contrast agents

1.1.1 T1 and T2 weighted MRI

As illustrated in Figure 1a, upon exposure to an external magnetic field (B_0), a greater proportion of protons will prefer to align parallel to the magnetic field (lower energy state), while the remainder aligns antiparallel (higher energy state). Therefore, a net magnetization (M_z) is produced along the direction of magnetic field (z-axis), and protons spin around the z-axis at a precession rate named the Larmor frequency (ω_0). During this period, protons precess separately (out of phase). When an RF pulse is applied to the nuclei with the same precession frequency, some protons in the lower energy state are flipped to the higher state by absorbing the RF energy (Figure 1b). Furthermore, the protons become synchronized and precess together (in phase). Consequently, a transverse magnetization (M_{xy}) perpendicular to the static magnetic field is generated.

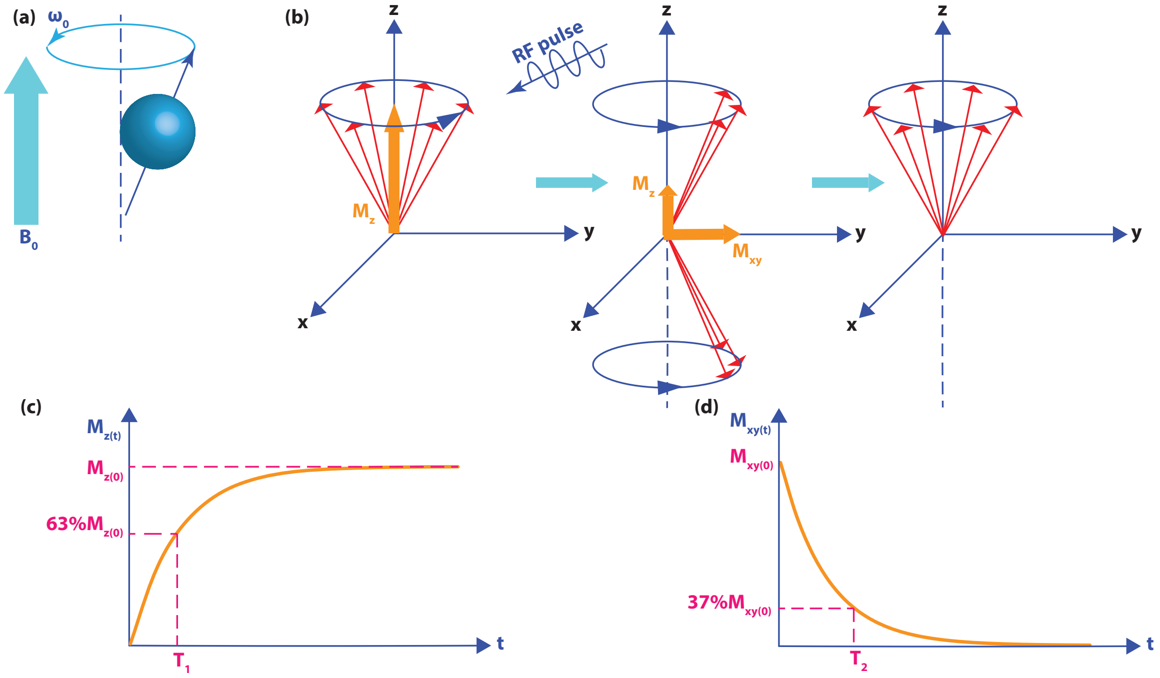

Figure 1. The principles of magnetic resonance imaging. a) Protons align either parallel (majority) or antiparallel (minority) and precess under external magnetic field B_0. b) Upon the introduction of RF pulses, protons are excited, with relaxation occurring following removal of the RF pulses. Graphical representation of c) T_1 relaxation (eqn (1)) and d) T_2 relaxation (eqn (2))[1].

After removal of the RF pulse, the protons relax to their equilibrium state via two relaxation pathways: longitudinal relaxation (T_1 relaxation) and transverse relaxation (T_2 relaxation). In T_1 relaxation, antiparallel protons jump back to the parallel state and give up energy to molecules in the surrounding environment (lattice), so that T_1 relaxation is known as spin-lattice relaxation. The recovery of M_z is described in equation below (1), where the T_1 relaxation time is defined as the time taken to recover 63% of the original longitudinal magnetization. The T_1 relaxation rate, R_1, is given by the reciprocal of T_1 ($1/T_1$), which is a function of r_1 (T_1 relaxivity), an intrinsic property of T_1 contrast agents, and contrast agent concentration (see equation (2)). The ideal T_1 contrast agents should be able to effectively shorten the T_1 relaxation time at low concentration. In terms of T_2 relaxation (spin-spin relaxation), protons that are in phase begin to dephase, with the transverse magnetization (M_{xy}) decaying as a result. This decay process follows equation (3), where T_2 refers to the time taken to decay to 37% of the original M_{xy} value. T_2 relaxivity (r_2), an intrinsic property of T_2^* contrast agents, affects the T_2 relaxation rate, R_2, as described in equation (4). Generally, spins decay faster than T_2 due to the magnetic field inhomogeneity generated by T_2 contrast agents. After taking this inhomogeneity into consideration, the effective relaxation time (T_2*) is given by equation (5), where γ is the gyromagnetic ratio and ΔB_i is the difference in the local magnetic field strength due to the inhomogeneity.

$$\boldsymbol{M_{z(t)} = M_{z(0)}\left[1 - \exp\left(-\frac{t}{T_1}\right)\right]} \qquad \textbf{(1)}$$

$$\boldsymbol{R_1 = \frac{1}{T_1} = \frac{1}{T_{1,H_2O}} + r_1[C]} \qquad \textbf{(2)}$$

$$\boldsymbol{M_{xy(t)} = M_{xy(0)}\exp\left(-\frac{t}{T_2}\right)} \qquad \textbf{(3)}$$

$$\boldsymbol{R_2 = \frac{1}{T_2} = \frac{1}{T_{2,H_2O}} + r_2[C]} \qquad \textbf{(4)}$$

$$\boldsymbol{\frac{1}{T_2^*} = \frac{1}{T_2} + \gamma\Delta B_i} \qquad \textbf{(5)}$$

1.1.2 Chemical Exchange Saturation Transfer

The contrast of chemical exchange saturation transfer (CEST) is generated through chemical exchange between solute and solvent, and can be proton or small molecule exchange (Figure 2e–i)[2]. The simplest model used to describe this process is the two-pool model, shown in Figure 2[3]. The exchangeable solute protons are selectively saturated by radiofrequency (RF) irradiation, and the saturated solute protons are subsequently transferred to bulk water protons by the exchange process, so that the signal of bulk water is attenuated. Since the water pool (concentration of about 110 M) is much larger than the solute pool (concentration in micromolar to millimolar range), each presaturated solute proton will be replaced by a non-saturated bulk water proton, and therefore another exchange occurs. With a fast exchange rate and long saturation time, this process will be continually repeated, with the bulk water signal becoming increasingly attenuated.

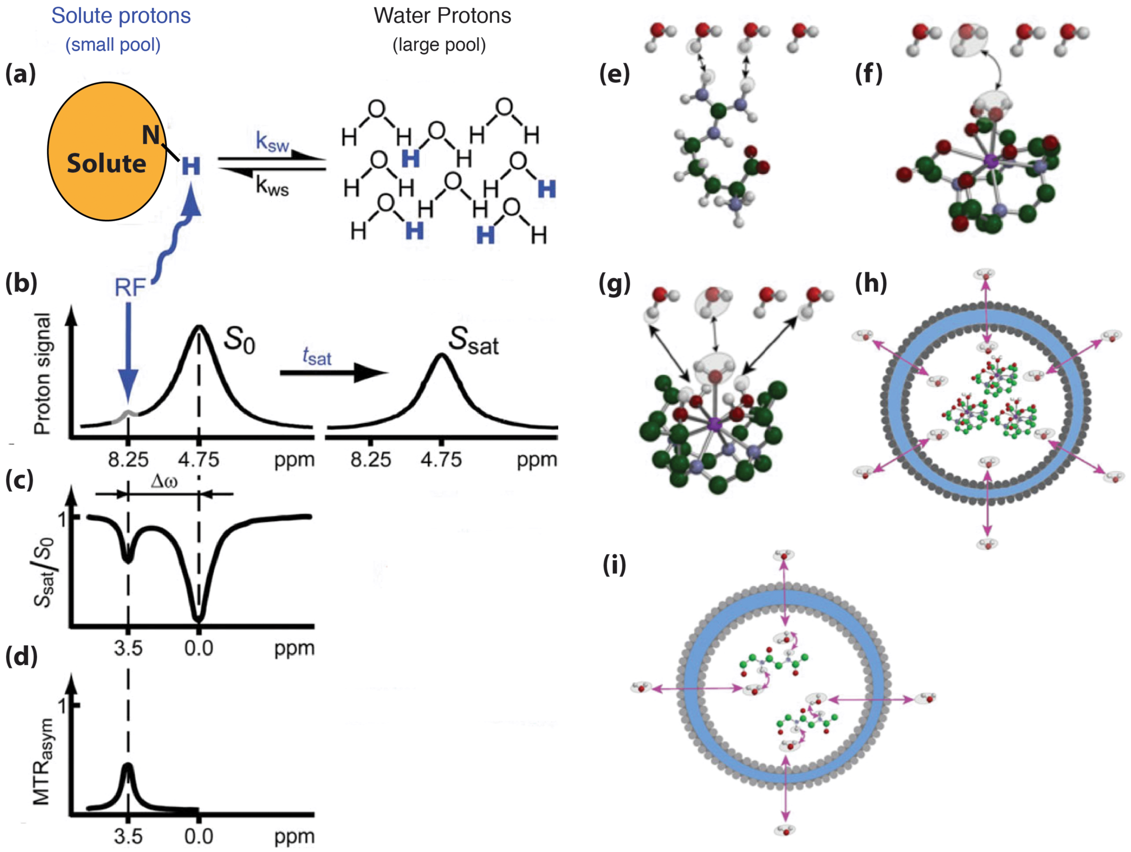

Figure 2. CEST principle. (a) Exchangeable solute protons are selectively saturated at a specific resonance frequency (RF) (8.25 ppm for amide protons), and the saturation is subsequently transferred to water (4.75 ppm). Non-saturated protons (black) are replaced by saturated solute protons (blue), and the process will be repeated to generate a discernable effect on the water signal intensity. (b) The saturation transfer causes water signal attenuation after t_{sat}. (c) Z spectrum (or CEST spectrum, MT spectrum). When RF irradiates at 4.75 ppm, the water signal disappears because of direct saturation (DS), and the frequency is set to 0 ppm in Z spectrum. After a period of RF saturation (t_{sat}), CEST effect becomes obvious, and the frequency of solute protons (amide protons) is 8.25–4.75 = 3.5 ppm. (d) MTR_{asym} spectrum: asymmetry analysis of Z spectrum to remove DS effect. Various exchange pathways: (e) proton exchange, (f) molecule exchange, (g) proton and molecule exchange, (h) compartment exchange, and (i) molecule-mediated compartment exchange[1].

1.2 Self-assemblies for MRI

Magnetic resonance imaging (MRI), developed on the principle of nuclear magnetic resonance (NMR), is one of the most powerful tools extensively used for noninvasive molecular and cellular imaging[4]. With superb spatial resolution and tissue contrast, MRI provides anatomic images of soft tissues and is considered as one of the most important diagnostic modalities for imaging of the brain[5], cartilage, heart, blood vessels and for tumor detection[6]. Unlike other imaging platforms, such as computerized axial tomography (CAT), positron emission tomography (PET) and single-photon-emission computed tomography (SPECT), MRI techniques do not require the use of radioactive agents and ionizing radiation. Although MRI itself is able to provide detailed images of soft tissues, its intrinsic low sensitivity makes it hard to differentiate normal tissues from lesions. The introduction of supplements, called contrast agents, can enhance the contrast effect at regions of interest by accelerating magnetic relaxation[7, 8]. These MRI contrast agents can be divided into three groups based on the mechanism by which contrast is generated. T_1 agents provide positive contrast by shortening the longitudinal relaxation time of surrounding water molecules, whereas T_2 agents shorten the transverse relaxation time of water protons. The third group relies on chemical exchange saturation transfer (CEST) and represents a relatively new approach to enhance MRI contrast. CEST agents exchange their presaturated exchangeable protons with those of bulk water, with the MRI contrast capable of being switched "on" and "off" by irradiation with radiofrequency (RF) pulses.

Among the various contrast agents, nanoparticle-based contrast agents (especially nanoparticles with diameters of 1–100 nm) have become extremely attractive due to their unique features. Firstly, nanoparticles can be loaded with up to hundreds of thousands of imaging moieties per structure, providing superb signal amplification that enables good imaging contrast at a low dose of contrast agent, and reduces the potential for any cytotoxicity associated with the contrast agent[9]. For example, a 150 nm dendrimer nanocluster possesses a loading capacity of ~300,000 gadolinium ions, giving a r_1 relaxivity value of 12.3 $mM^{-1}sec^{-1}$ per gadolinium ion and 3,600,000 $mM^{-1}sec^{-1}$ per particle (1.41 T, 40 °C)[10], while the r_1 relaxivity value of small gadolinium chelates is only 3.5 $mM^{-1}sec^{-1}$. Secondly, compared to bulk counterparts, nanoparticles possess a relatively large surface area that offers improved reactivity and an ability to be tailored with additional surface moieties to either improve targeting[11] or introduce additional functionality (such as therapeutic features[12] or fluorescence[13]). Multimodal MRI contrast agents are even more prevalent since they can reveal several properties at the same site by applying a single contrast agent. Thirdly, nanoparticles tend to accumulate at tumor sites through the enhanced permeability and retention (EPR) effect[14], thereby rendering a higher signal-to-noise ratio in tumors[15].

Researchers have developed various types of nanoparticle-based MRI contrast agents of T_1, T_2 and CEST modalities to fulfill different purposes. Among them, T_1 nanoparticle-based contrast agents have proven the most popular due to the positive contrast provided. Gadolinium (Gd^{III}) complexes like Gd-DTPA are widely used to detect the breakage of the blood brain barrier (BBB) and characterize changes in vascularity[16]. However, Gd^{III} chelates have a short circulation time and the relaxivity exhibited is relatively low, requiring a large dose of ion chelates to reach a useful detection level. Moreover, the non-biocompatible gadolinium has the potential to introduce toxicity into cells upon dechelation from its complexes. Alternatively, nanostructures (like dendrimers[17], liposomes[18], quantum dots[19], mesoporous silica[20] and carbon nanotubes[21]) can be employed as carriers for $\mathrm{Gd^{III}}$ chelates, which significantly improves relaxivity, and the nanoparticle surface can be facilely modified with additional functional groups to create multimodal contrast agents. As members of soft nanoparticles, supramolecular self-assemblies based MRI contrast agents have quickly drawn researchers' attention since their first introduction by Stupp and Meade[22], where self-assembling peptide amphiphiles (PAs) were conjugated with macrocyclic $\mathrm{Gd^{III}}$ chelates to furnish peptide-amphiphile based T1 MRI contrast agents (PACAs). Nanostructures self-assembled from PAs can emulate extracellular matrices, a biomimetic strategy widely applied in the field of regenerative medicine[23]. Depending on the design rationale and assembly environment, various one-dimensional morphologies with different physical properties can be obtained upon self-assembly of PAs, which renders PACAs a versatile platform for imaging purposes[24]. Most importantly, it is well known that the relaxivity of contrast agents will be enhanced by conjugation to proteins and polymers with large molecular weight, or by preparation of micellar structures[25]. Similarly, the structure of self-assembled PAs allows the increase in rotational correlation time (τ_r) that subsequently enhances relaxivity. Bull et al. reported the relaxivity difference that arose from the varying morphology of two self-assembled PAs (Figure 3a,b), where the relaxivity of nanofibers was 14.7 $\mathrm{mM^{-1}sec^{-1}}$, while the relaxivity of spherical micelles was 22.8 $\mathrm{mM^{-1}sec^{-1}}$ before cross linking (pH = 7.41)[26], both of nanostructure dramatically improved T_1 sensitivity compared with small molecular $\mathrm{Gd^{III}}$ chelates ($r_1 \sim 3.5\ \mathrm{mM^{-1}sec^{-1}}$).

MRI has also been used to image self-assembled hydrogel in Bull's work. Bull et al. fabricated three molecules (**1, 2, 3**) with similar sequences (Figure 3c,d), with PA **1** able to form self-supporting hydrogels, while PACAs **2** and **3** possessed Gd-DOTA positioned at different distances from the hydrophobic alkyl tails. Both PACAs self-assembled into nanofibers at pH greater than 7.0, though cannot form hydrogels by themselves[22]. Upon mixing PACA **2** or **3** with filler PA **1**, a homogeneous hydrogel was formed that allowed MR images to be obtained. From the MR images of these phantom gels, the mixture of PACA **3** and PA **1** exhibited the greatest contrast, implying that positioning Gd^{III} chelates closer to the hydrophobic end of PAs would result in higher relaxivity. The postulated reason behind this was due to the decreased internal flexibility and increased steric hindrance of Gd^{III} chelates that occurs upon self-assembly. Since the highest contrast was generated with PACA **3**, it was further mixed with various epitope-bearing PAs (such as the IKVAV or YIGSR epitopes for neuronal stem cell differentiation, and the RGD epitope for cell adhesion) to form hydrogels (doping with an equal amount of **3**). The T_1 values of each mixed hydrogel were found to be similar, proving the ubiquitous ability to use PACAs with various PA gels.

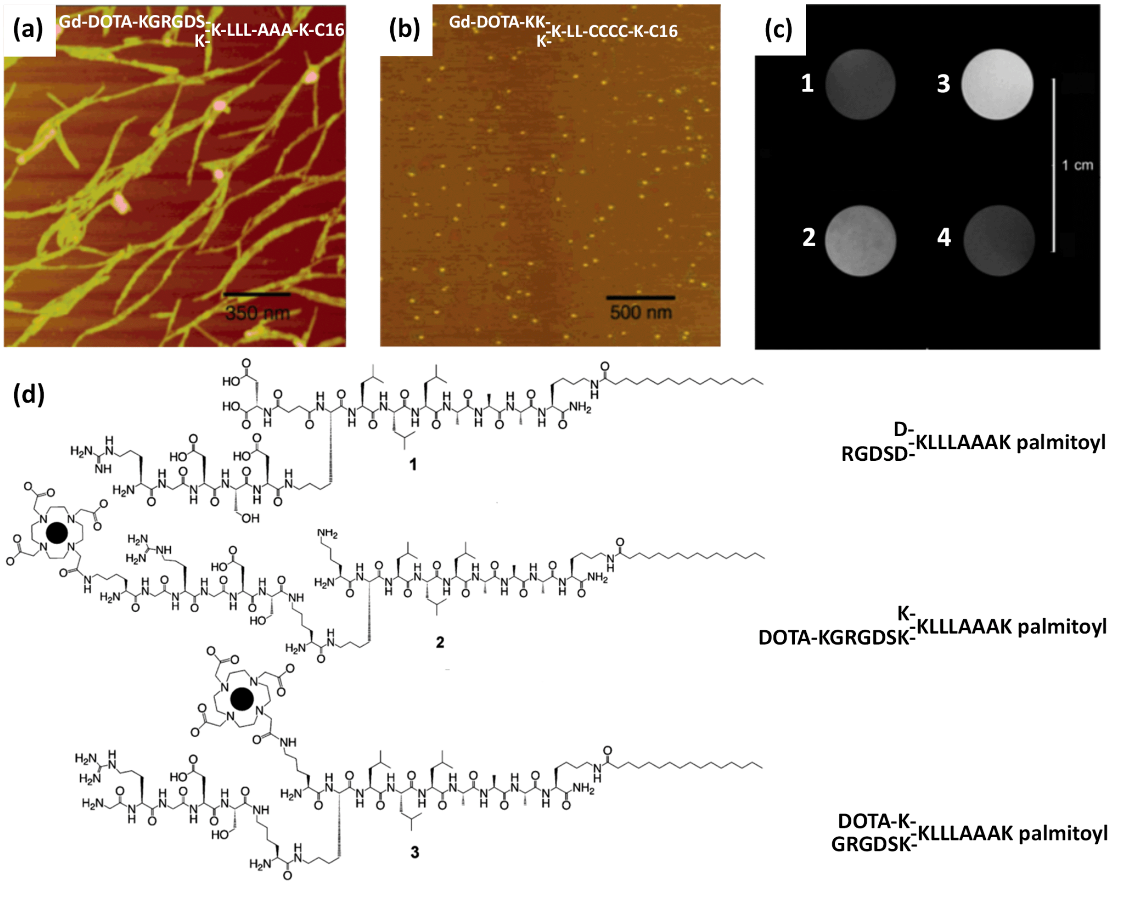

Figure 3. Self-assembled peptide amphiphile nanofibers conjugated with Gd-based magnetic moieties. a) AFM image of nanofibers. b) Atomic force microscopy (AFM) image of

nanospheres. c) Molecular design of 1, 2, 3. d) MR images of phantom gels formed from (1) the control PA of 1, (2) a mixture of 1 and 2, (3) a mixture of 1 and 3, and (4) Gd-DTPA. The mixture of 1 and 3 demonstrated the highest contrast due to the increase in τr of Gd^{III} chelates[1].

What's more, the feasibility of employing supramolecular dual-modality nanoprobes (self-assembly of amphiphilic peptide conjugates containing the fluorophore 5-FAM and Gd-DOTA) as contrast agents for MR and fluorescence imaging was assessed by Cui and co-workers (Figure 4)[27]. The live-cell fluorescence imaging of two self-assembled nanoprobes (one with single hydrocarbon tail, and the other with two hydrocarbon tails) was studied in KB-3-1 human cervical cells to evaluate cell viability of PACAs. The dual-tailed PACA 2 (50 μM) showed 25-fold higher cellular uptake than PACA 1 (200 μM), which was due to membrane insertion through the two hydrophobic alkyl chains. Before self-assembly, the relaxivity, r_1, of PACA 1 and PACA 2 were 4.3 $mM^{-1}sec^{-1}$ and 4.2 $mM^{-1}sec^{-1}$ (pH = 7.4, room temperature), respectively, which were similar to the relaxivity of small molecular Gd-DOTA contrast agents (3.5–4.8 $mM^{-1}sec^{-1}$)[28]. However, upon self-assembly, the nanospheres formed by PACA 1 and PACA 2 had relaxivities of 7.8 $mM^{-1}sec^{-1}$ and 14.3 $mM^{-1}sec^{-1}$ that were higher than the monomeric forms. The higher relaxivity of self-assembled PACA 2 stems from the denser packing of PACA 2 in its self-assembled state, which led to a higher aggregation number of molecules and effective molar mass than self-assembled PACA 1.

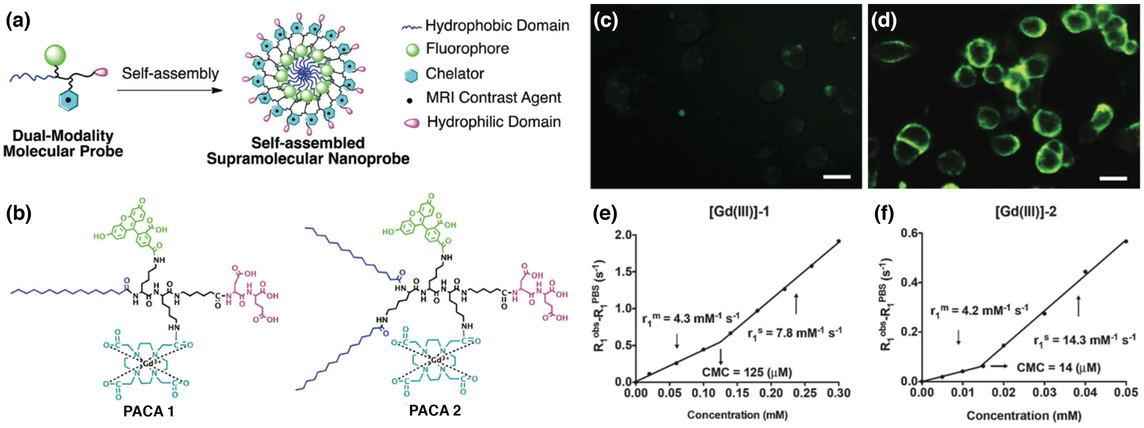

Figure 4. Dual-modal supramolecular nanoprobes. a) Rational design of supramolecular dual-modality nanoprobes, composed of a hydrophobic domain to promote self-assembly, a

fluorophore for optical imaging, a GdIII chelator for MR contrast, and a hydrophilic headgroup. b) Chemical structures of PACA 1 and PACA 2. Fluorescence images of KB-3-1 cells after incubation (2h) with c) PACA1 (200 μM) and d) PACA2 (50 μM). Scale bars were 20 μm. e)-f) The plots of $1/T_1$ versus concentration for [Gd (III)]-1 and [Gd (III)]-2. Slopes as r1[1].

As we described above, self-assembling PAs have the propensity to enhance T_1 relaxivity, and one advantage associated with fibrous PA structures is their potential for biodegradation into natural building blocks, so that it is of importance to track the fate of biomaterials after implanted *in vivo*[29]. There are, however, limited studies that shed light on the degradation process *in vivo*. By incorporating MRI modality to image PACAs, we could rationalize using PACAs to enhance MRI contrast, and possibly allow us to track the fate of PACAs *in vivo*, thus laying a critical foundation for future development as therapies[30]. Stupp, Meade and co-workers have reported on the *in vivo* biomaterial localization with Gd(HPN_3DO3A) labelled peptide nanofibers (Figure 5). These PAs were designed to have one chelate next to the *C*-terminal (PA1 and PA2), three chelates at the *C*-terminal end (PA3), or one chelate relatively far away from the *C*-terminus (PA4)[29]. Small-angle X-ray scattering (SAXS) experiments revealed that the bulky Gd (HPN_3DO3A) conjugated to the outermost residue of the PAs exhibited β-sheet character and retained high-aspect-ratio structures. The *in vivo* degradation was evaluated with the mixture (gels) of PA (1 or 3) and filler $C_{16}V_3A_3E_3$-NH_2, of which the PA1 gel produced positive contrast in T_1-weighted MRI and PA3 gel produced negative contrast. Subsequent ICP-MS analysis was conducted to measure Gd^{III} retention. The result showed that 62 ± 8% of PA1 and 54 ± 9% of PA3 remained in the mouse leg after 4 days, and the similar T_1 relaxation time at day 0 and day 4 indicated the PA concentration did not change significantly, verifying that the approach of using MRI to track the fate of biomaterials is practicable.

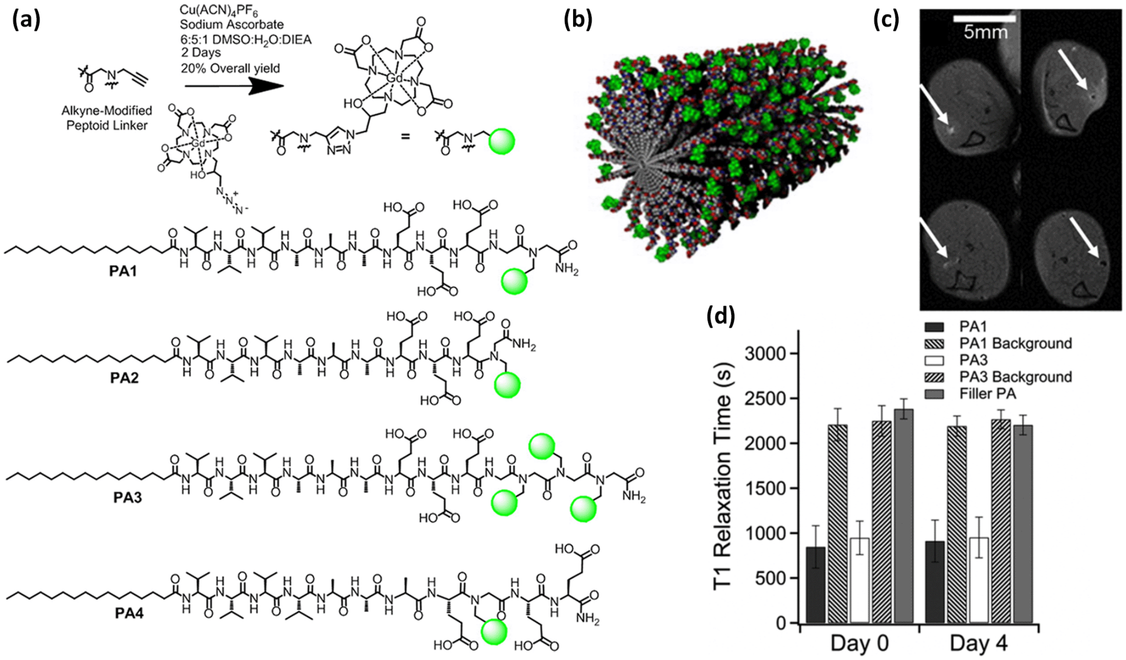

Figure 5. *In vivo* biomaterial localization with Gd-labeled peptide nanofibers. a) Schematic illustration of the 'clicking' of Gd(HPN3DO3A) to the alkyne peptoid. Chemical structure of the self-assembling MRI contrast agents PA1–PA4. b) Cartoon of self-assembled nanofibers of PA1. *In vivo* evaluation of PA1 and PA3: c) 4 uL of PA gels were injected into each of six wild-type mice (injection point indicated by white arrows), and anatomical scan of mouse legs was performed immediately upon injection (top row) and after 4 days (bottom row). PA1 produced positive contrast in T_1 weighted MRI, while PA3 produced negative contrast in T_2 weighted MRI. d) Average T_1 times from the region of interest and the background measured several millimeters from the PA injection site). PA1 possessed the shortest T_1 time (highest r1 relaxivity)[1].

Chapter 2: CEST MRI traceable self-assembling drug-peptide nanofiber

Over past decades, we witnessed remarkable development of drug delivery strategies. There are, however, remaining challenges that limit the efficacy of chemotherapeutic drugs in cancer treatment. Due to non-selective accumulation in healthy organs, such as kidney and liver spleen, only a small amount of drug arrive at targeted tumor site[31]. Besides, high interstitial fluid pressure (IFP) inside the tumor cells serves as a barrier for chemotherapeutic drugs intending to penetrate into the tumor cells, thus most of therapeutics only distribute around the peripheral of tumor[32]. Therefore, the ability to monitor and track therapeutic drugs is highly desirable to identify premature clearance, locate drug accumulation site and distribution, so as to achieve a better drug prognosis and to comprehend treatment failures[33]. To render real time reporting of drug circulation and distribution upon *in vivo* administration, image-guided drug delivery or theranostic systems have been widely explored to incorporate chemotherapeutic drugs with different imaging modalities such as PET[34], SPECT[35], MRI[36], and ultrasonic[37]. MRI is one of the most commonly used diagnostic methods thanks to its superior spatial resolution and soft tissue contrast. However, most currently available MRI contrast agents are made from metal-chelators such as gadolinium (Gd), which are highly toxic in their free ionic forms. It has been reported to trigger nephrogenic systemic fibrosis[38] and very recently was found to deposit even in the brain of patients without severe renal dysfunction[39].

Chemical Exchange Saturation Transfer (CEST) is an emerging MRI contrast mechanism, which utilizes special MRI pulse sequence to selectively detect exchangeable protons on each probe at their unique chemical shift (frequency offset), translating them into a frequency-specific molecular imaging agents.[40, 41] The exchangeable protons are detected by the attenuation of MRI (water) signal caused by the continuous transfer of the saturated (NMR signal being nulled) protons from the probes to their surrounding water molecules. Using the CEST approach, bio-organic molecules[42-45] containing exchangeable protons such as –O**H**, –N**H** and –N$\mathbf{H_2}$ groups can be saturated by a specific radiofrequency pulse. For example, a series of X-ray contrast agents, Iopamidol,[46] Iopromide,[47, 48] and Iobitridol[49] with –NH proton were shown to exhibit CEST MRI signal that enabled *in vivo* microenvironment pH mapping. More importantly, CEST potentially can also be used to detect therapeutic drugs[42, 50], drug/gene delivery systems[51, 52] and the subsequent tumor responses[53-55] in a "label-free" manner. One unbeatable advantage to use CEST MRI for pursuing image-guided drug delivery is that, with the intrinsically endowed CEST contrast, extensive chemical labelling of bioactive molecules can be avoided, namely "natural labelling".

Herein, we report an FDA-approved anticancer drug, Pemetrexed (**Pem**), marketed under the trade name Alimta,[56] has an inherent CEST MRI signal at 5.2 ppm frequency offset from the resonance of water. After being covalently linked a short peptide to form an amphiphilic **Pem-**peptide conjugate, the self-assembly of nanofibers hydrogel could be spontaneously formed, which is not only injectable for intra-tumor treatment but also detectable by CEST MRI. We demonstrated that the delivery and distribution of **Pem**-peptide nanofiber hydrogel can directly assessed by CEST MRI in a mouse glioma model.

Chapter 3: Materials and Methods

3.1 Synthesis and molecular characterization

3.1.1 Materials

Fmoc amino acids and Fmoc-Glu(OtBu)-Wang resin were purchased from Advanced Automated Peptide Protein Technologies (AAPPTEC, Louisville, KY). Pemetrexed (**Pem**) was purchased from AvaChem Scientific (San Antonio, TX). Lauric acid was purchased from Fisher Scientific (Pittsburgh, PA). Hydrochloric acid was purchased from EMD Millipore (Billerica, MA), and sodium hydroxide was purchased from Fisher Scientific (Fair Lawn, NJ).

3.1.2 Synthesis of PemFE and C12FE

The peptide Fmoc-FFEE was synthesized on a Focus XC automated peptide synthesizer (AAPPTEC, Louisville, KY) with the scale of 0.25 mmole by utilizing standard Fmoc-solid phase synthesis techniques. Fmoc deprotection was followed using 20% 4-methylpiperidine in DMF solution for 15 minutes, repeating once. After Fmoc deprotection, lauric acid was manually coupled to N-terminus of NH_2-FFEE at the ratio of Lauric acid/HBTU/DIEA 4:4:10 relative to the peptide, shaking overnight at room temperature. The coupling of **Pem** was performed manually at N-terminus of NH_2-FFEE by adding Pem/HBTU/DIEA at a ratio of 1.2:1.2:3 relative to the peptide, shaking overnight at room temperature. In all cases, reactions were monitored by the ninhydrin test (Anaspec Inc., Fremont, CA) for free amines. Both **C12FE** and **PemFE** were cleaved from the Wang resins using the standard cleavage solution of TFA/TIS/H_2O (92.5:5:2.5) for 2.5 hours. Excessive TFA was removed by air blow, and the remaining peptide solution was titrated with cold diethyl ether to precipitate crude peptide. The precipitated crude peptide and diethyl ether were phase-separated using centrifugation technique (5900 rpm for 3 minute) and diethyl ether solution was discarded. To remove as much TFA as possible, the washing step was carried out by adding 40 mL of diethyl ether to crude peptide, vortexed, sonicated and centrifuged. This procedure was repeated 3 times. All centrifuge tubes were tightly sealed with parafilm to minimize evaporation of diethyl ether during high-speed centrifugation. After centrifuge, the precipitate was dried under vacuum overnight.

3.1.3 Purification

The peptides were purified by preparative RP-HPLC with a Varian Polymeric Column (PLRP-S, 100 Å, 10 μm, 150 × 25 mm) at 25 °C on a Varian ProStar Model 325 preparative HPLC (Agilent Technologies, Santa Clara, CA) equipped with a fraction collector.

C12FE peptide was dissolved in 20 ml of 0.1% v/v NH_4OH. A water/acetonitrile gradient 5%-100% was ran for 30 minutes containing 0.1% v/v NH_4OH was used as eluent at a flow rate of 20 mL/min.

The crude **PemFE** peptide was initially dissolved in 20 ml of 0.1% v/v NH_4OH, then diluting with 20 ml of 0.1% v/v TFA. A water/acetonitrile gradient 5%-50% was ran for 30 minutes containing 0.1% v/v TFA was used as eluent at a flow rate of 20 mL/min.

The absorbance peak was monitored at 220 nm. Peptide identity was confirmed by ESI-MS (LDQ Deca ion-trap mass spectrometer, Thermo Finnigan, San Jose, CA). Collected fractions containing desired products were lyophilized (FreeZone -105 °C 4.5 L freeze dryer, Labconco, Kansas City, MO) and stored at -30 °C.

3.1.4 Electrospray Ionization-Mass Spectra (ESI-MS)

ESI mass spectra were acquired using a Finnigan LCQ Deca ion-trap mass spectrometer equipped with an electrospray ionization source (Thermo Finnigan, San Jose, CA). Samples were dissolved in water with 5% of acetonitrle containing 0.1% v/v NH_4OH and introduced into the instrument at a rate of 10 μL/min using a syringe pump via a silica capillary line. The heated capillary temperature was 250 °C and the spray voltage was 5kV.

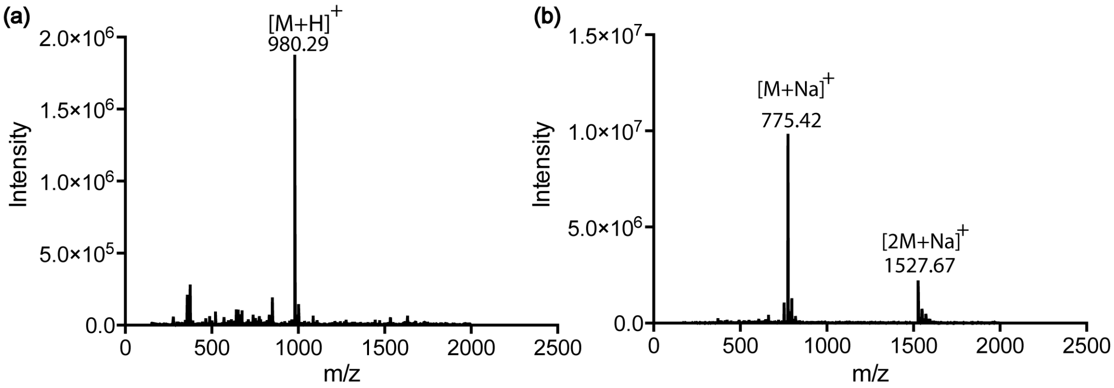

Figure 6. ESI-MS of a) PemFE and b) C12FE molecules. The exact mass of PemFE and C12FE are 979.37 and 752.40, respectively.

3.1.5 Analytical HPLC Characterization

Analytical RP-HPLC was performed using a Varian polymeric column (PLRP-S, 100 Å, 10 μm, 150 × 4.6 mm) with 20 μL injection volume. A water/acetonitrile gradient 5%-100% was ran for 30 minutes containing 0.1% v/v NH_4OH at a flow rate of 1 mL/min.

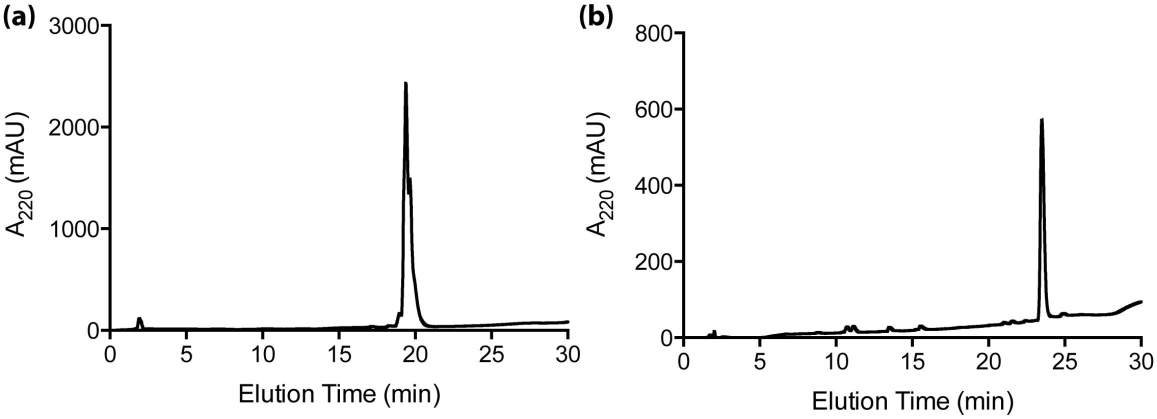

Figure 7. Analytical RP-HPLC of a) PemFE and b) C12FE. PemFE isomer resulted in a shoulder peak in plot a).

3.1.6 PemFE Isomer

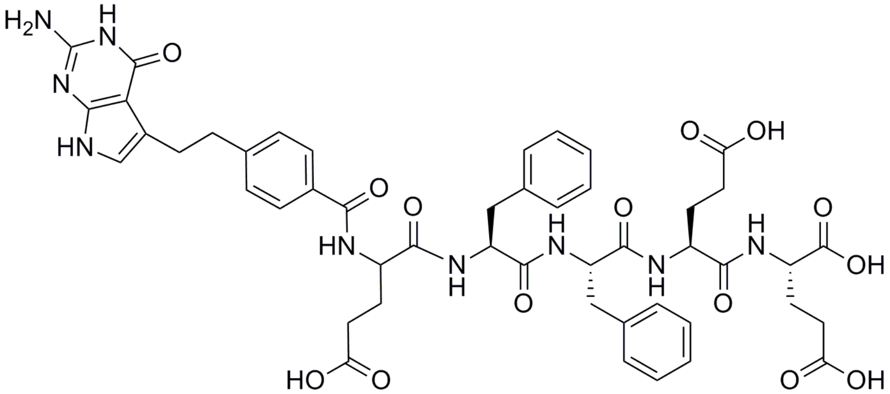

Figure 8. Chemical structure of PemFE isomer.

3.1.7 Drug loading for PemFE

Pem mass = 427.4 g/mol – 17 g/mol (-OH) = 410.4 g/mol

PemFE mass = 979.3 g/mol

PemFE drug loading = 410.4/979.3 × 100% = 41.9%

3.2 Self-assembly characterization

3.2.1 Transmission electron microscopy (TEM) imaging protocol

4 mM solutions of **C12FE** and **PemFE** in 1xDPBS were prepared by directly dissolving lyophilized powders, and allowed to age overnight. A sample for imaging was prepared by depositing 5 μL of the solution onto a carbon-coated copper grid (Electron Microscopy Services, Hatfield, PA, USA), wicking away the excess solution with a small piece of filter paper. Next, 5 μL of a 2 wt % aqueous uranyl acetate solution was deposited and the excess solution was carefully removed as above to leave a very thin layer. The sample grid was then allowed to dry at room temperature prior to imaging. Bright-field TEM imaging was performed on a FEI Tecnai 12 TWIN Transmission Electron Microscope operated at an acceleration voltage of 100 kV. TEM images were recorded by a 16 bit 2K × 2K FEI Eagle bottom mount camera.

3.2.2 Cryogenic TEM protocol

To visualize nanostructures in its solution-state through a vitrified thin-film, cryo-TEM imaging was performed on the FEI Tecnai 12 TWIN Transmission Electron Microscope, operating at 80 kV. **C12FE** and **PemFE** samples were prepared at 4mM in PBS, the same concentration as conventional TEM. Prior to sample preparation, all TEM grids were treated with plasma air to make the lacey carbon film hydrophilic. The Vitrobot with a controlled humidity chamber (FEI) was used to generate a thin film of sample on grid. The lacey carbon grid (Electron Microscopy Services, Hatfield, PA) was blotted and plunged into liquid ethane pre-cooled by liquid nitrogen. All vitrified samples were transferred to a cryo-holder filled with liquid nitrogen to prevent sublimation of vitreous water. The images were recorded by a 16 bit 2K × 2K FEI Eagle bottom mount camera.

3.3 *In vitro* MRI CEST measurement

In vitro CEST MRI images were acquired on a 9.4T Bruker Avance system equipped with a 15 mm sawtooth RF coil. A modified RARE sequence (TR=6.0 sec, effective TE=43.2 ms, RARE factor=16, slice thickness=1 mm, FOV=14x14 mm, matrix size=128x64, resolution= 0.11x0.22 mm^2, and NA=2) including a magnetization transfer (MT) module (one CW pulse, B =3.6 µT (150 Hz), 3sec) was used to acquire CEST weighted images from -7 ppm to 7 ppm (step=0.2 ppm) around the water resonance (0 ppm)[57]. The absolute water resonant frequency shift was measured using the WAter Saturation Shift Reference (WASSR)[58] method modified with Lorentzian analysis. The same parameters as in CEST imaging were used except TR=1.5 sec, t_{sat}=500 ms, B_1=0.5 µT (21.3 Hz) and the saturation frequency swept from -1ppm to 1ppm (step= 0.1 ppm).

Data processing was performed using custom-written scripts in MATLAB (Mathworks, Waltham, MA). CEST spectra were calculated from the mean of an ROI placed over each sample after B_0 correcting the contrast on a per voxel basis. The CEST signal was quantified using

MTR_{asym} at particular offsets of interest (i.e. Δω= +2.2 ppm) using the definition: $MTR_{asym} = (S^{-\Delta\omega} - S^{+\Delta\omega})/ S_0$, where and $S^{[-\Delta\omega,\ +\Delta\omega]}$ is the water signal intensity in the presence of saturation pulse at offsets ±Δω, and S_0 is the water signal intensity in the absence of saturation pulses.

C12FE, **PemFE** and **Pem** samples were prepared at 10mM in 1xDPBS solution. A pH series ranging from 6.0 to 8.5 with an increment of 0.5 was studied, and sodium hydroxide or hydrochloric acid solution was used to achieve expected pH. 1 M solution of sodium hydroxide was prepared by dissolving solid sodium hydroxide in deionized water, while 11 M hydrochloric acid was diluted with water to 1 M hydrochloric acid. Samples were triplicated at each pH. After pH adjustment, samples were transferred to capillary tubes and then arranged on a sample holder.

The exchange rates of exchangeable protons of 10 mM **Pem**, **PemFE** and **C12FE** at different pHs were measured using the modified QUantifying Exchange using Saturation Time (QUEST) method[59]. In brief, the CEST contrast at 5.2 ppm for each sample was measured with saturation delays of 0.5, 1, 1.5, 2, 3 and 6 sec, using a saturation field strength of 4.7 µT (200Hz) and the repetition time (TR) set to 10 sec, using the RARE imaging sequence described previously. The calculated MTR_{asym} values were then fit using numerical solutions to the Bloch equations with exchange rate (k_{ex}). The water T1w and T2w were experimentally determined using a saturation recovery spin echo method and CPMG multi-echo spin echo sequence respectively. The fixed model parameters were water solute R1s= 0.71 Hz and solute R2s= 39 Hz.

3.4 PemFE and C12FE hydrogels

PemFE and **C12FE** hydrogel were prepared in the final concentration of 30 mM, dissolved in 1xDPBS solution and sonicated for 2 minutes to aid in dissolving lyphophilized powder form of respective molecules. Samples were aged overnight and hydrogel photos were taken by inverting both sample vials.

3.5 *In vivo* MRI study

All experiments conducted with mice were performed in accordance with protocols approved by the Johns Hopkins University Institutional Animal Care and Use Committee (IACUC). *In vivo* images were acquired on an 11.7 T Bruker Biospec horizontal bore scanner (Bruker Biosciences, Billerica, MA) equipped with a 23 mm Circular Polarized MRI transceiver volume coil. The same imaging scheme described above with addition of a fat suppression pulse (3.4 ms hermite pulse, offset=-3.5 ppm). The acquisition parameters were: TR=5.0 sec, effective TE= 6 ms, RARE factor=10, t_{sat}=3 sec, B_1=3.6 μT (150 Hz), slice thickness=1 mm, acquisition matrix size=128x64, FOV=20x20 mm, and NA=2. Due to the B_0 field inhomogeneity, we incremented the saturation offset ± 1 ppm (0.1 ppm steps) with respect to water for B_0 mapping.

Chapter 4: Results and Discussion

4.1 Molecular Design

Pemetrexed (**Pem**) is a chemotherapeutic drug composed of aromatic amines and secondary amines in its nature structure (**Pem** in blue, Figure 9a). These exchanging protons posses a chemical shift (5.2 + 4.7 ppm, by NMR convention) distinct from water, in which can be selectively saturated and transferred to bulk water through chemical exchange, resulting in a decrease of water signal (Figure 9b). Subsequently, the decrease in water signal "before" and "after" the application of saturation RF pulses is computed as the magnetization transfer ratio (MTR_{asym}), providing a way to quantify the CEST effect corresponded to the amount of **Pem**. Thus, **Pem** can be used as a CEST MRI contrast agent. Because **Pem** (Figure 9a) is a hydrophobic anticancer drug, based on our previous studies[60-63], it has the potential to self-assemble into nanofibers under physiological condition (Figure 9c). To construct the Pem-peptide nanostructure, we chemically conjugated it to a hydrophilic peptide, two glutamic acids (EE), to create an amphiphilic prodrug molecule that can self-assemble into nanostructure[64, 65]. Glutamic acid residues, which carry negative charge on its side chain, are deliberately included in our design to minimize the ionic-induced cytotoxic effect commonly reported in positively charged nanoparticles.[66] To promote the self-assembly of **PemFE** into nanofibers hydrogel, two phenylalanine (FF) was incorporated into the peptide sequence. The phenylalanine benzyl side chain that composed of π-segment, was shown to direct the self-assembly of amphiphilic peptide into 1-dimensional nanostructures, such as nanotubes or nanofibers through π-π stacking[67, 68]. With this drug-peptide conjugate design, the **Pem** drug loading can be precisely fixed at 42 wt% which is defined by the mass of **Pem** divided by the total molecular weight of **PemFE** conjugate (as discussed in Material and Method 3.1.7). Our previous work[64, 65, 69] also demonstrated that this concept can be employed for other anticancer drugs to achieve higher drug loading compared to tradition drug encapsulation method (<5 wt%) and drug-polymer conjugate approach (~10 wt%)[70].

Due to the dual carboxylic acid functional sites on the **Pem**, our designed molecule **PemFE** possibly co-exist with its structural isomer as denoted by asterisk (*) in Figure 9a. Since the aromatic amine site is preserved in both **PemFE** and its structural isomer, we presumed that their CEST properties are unaffected. As a control molecule, we designed the **C12FE** molecule (Figure 9a), by replacing **Pem** drug with a C12-hydrocarbon tail as the hydrophobic entity to facilitate the self-assembly process of nanofiber formation, providing the physical feature similar to **PemFE**.

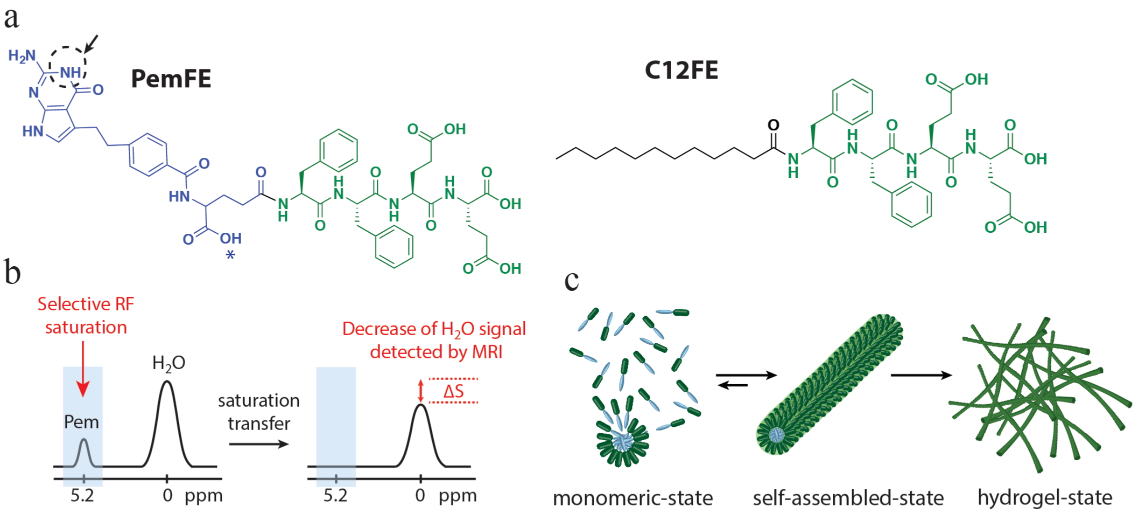

Figure 9. Illustration of Molecular Design. a) Chemical structure of molecule PemFE and C12FE, where the CEST MRI signal of PemFE originates from aromatic amine exchanging proton on Pem (blue). A possible PemFE structural isomer conjugation site is indicated by asterisk (*). b) CEST contrast is measured by a decrease in water signal after the selectively saturated 5.2 ppm exchanging proton is being transferred to bulk water. c) Illustration of PemFE monomers self-assembled into nanofiber and hydrogel-state.

4.2 Molecular self-assembly and characterization

The self-assembly of **PemFE** and **C12FE** were initiated by dissolving the lyophilized molecules into Dulbecco's phosphate-buffered saline (1xDPBS). The self-assembled nanostructures were observed under vitrified liquid using cryo-Transmission Electron Microscopy (TEM) without staining and regular TEM with negative staining. In Figure 10b, e, cryo-TEM micrographs showed that both **PemFE** and **C12FE** molecules self-assembled into cylindrical-shaped nanofibers in physiological buffer (1xDPBS) at 4 mM concentration (per conjugate), after aged for 1 day at room temperature. According to the diameter analysis of **PemFE** and **C12FE** nanofibers obtained from TEM images (Figure 10a, d), their respective diameters are 9.1 ± 1.4 nm and 8.5 ± 0.9 nm. The diameters of these nanofibers which correspond to approximately twice of the expected molecular length (~3.9 nm and ~3.2 nm, respectively, estimated from ChemDraw), indicating a core-shell packing model assembled into a cylindrical geometry. In addition, the lengths of these nanofibers are in the micrometer range, which form a dense nano-fabric network at high concentration. Consequently, at macroscopic level, **PemFE** and **C12FE** exist as self-supporting hydrogels at 30 mM in 1xPBS solution as shown in Figure 10c and 10f, respectively. This class of self-assembling hydrogel has emerged as a versatile strategy for slow release of bioactive molecules, an unique alternative in drug-delivery systems.[71-73] Due to the non-covalent interactions among nanofibers, this type of hydrogel is also injectable under proper shear stress and would recover back to its gel state after injection, which is highly desirable for *in situ* applications[74].

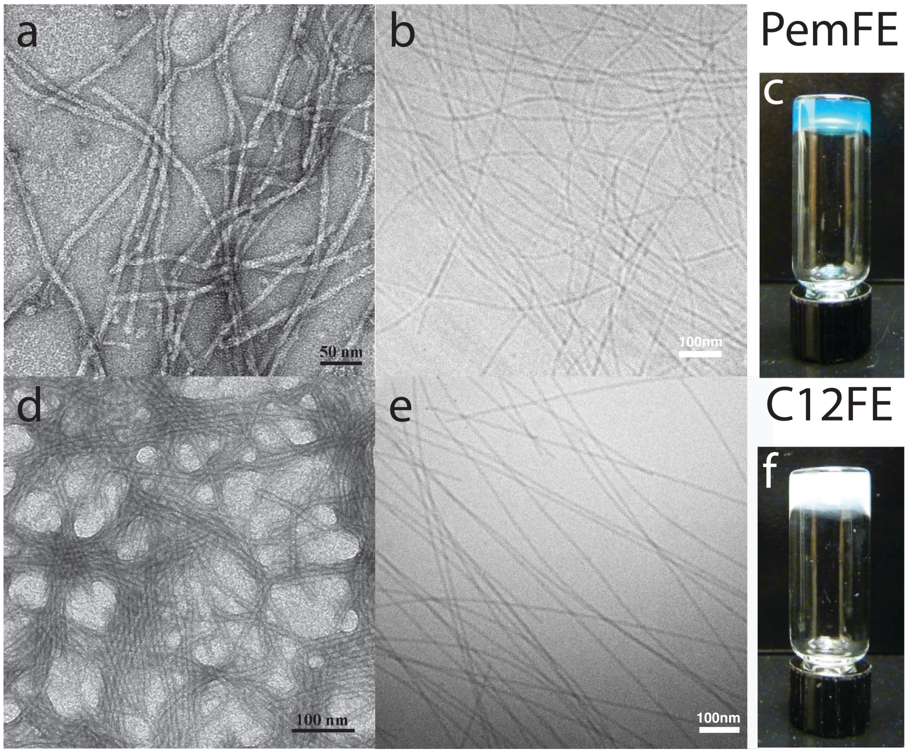

Figure 10. Demonstration of nanostructure formed by **PemFE** and **C12FE.** a) b) Cryo-TEM micrograph and regular TEM micrograph of **PemFE**, 4mM. c) Digital photographs of **PemFE** in 30 mM dissolved in 1xDPBS solution and aged overnight: inversion demonstrates self-supporting hydrogel formed by **PemFE** nanofibers. d) e) Cryo-TEM micrograph and regular TEM micrograph of **C12FE**, 10mM. f) Digital photographs of **PemFE** in 30 mM dissolved in 1xDPBS solution and aged overnight: inversion demonstrates self-supporting hydrogel formed by **C12FE** nanofibers.

4.3 *In vitro* CEST MRI Measurement

MRI contrast measurements revealed that **Pem**-containing molecules generate a strong CEST signal at ~5.2 ppm, while the control molecule **C12FE** showed negligible CEST signal at pH 7.4. We first prepared **PemFE**, **C12FE** and **Pem** at 10 mM concentration (in PBS, pH 7.4, and 37 ^{o}C) and measured their CEST properties on a 9.4 T vertical bore Bruker MRI scanner using a previously reported procedure[75]. The CEST effect was displayed as Z-spectra (Figure 11a) and further quantified using MTR_{asym}(Figure 11b), as defined by $MTR_{asym}=(S^{-\Delta\omega} - S^{+\Delta\omega})/ S_{0,}$ where $S^{-\Delta\omega}$ and $S^{+\Delta\omega}$ are the MRI signal intensities after saturation at $-\Delta\omega$ and $+\Delta\omega$ frequency offsets from the water proton frequency (set at 0 ppm); S_o is the intensity in the absence of a saturation pulse. Both Z-spectra and MTR_{asym} plots clearly showed a strong CEST signal at ~5.2 ppm. At this frequency offset, as shown in the color-coded CEST parametric map (Figure 11e), a conspicuously different CEST signal can be detected between **PemFE** and the control molecule **C12FE**. We speculate this CEST signal arises from the aromatic primary amine's exchanging proton on the **Pem** molecules (~10.15 ppm using ^{1}H NMR spectrometry[76]). It should be noted that, due to the fast exchange rate, the CEST peak at 5.2 ppm is broad and the exact offset to obtain the 'peak' CEST effect was observed to be slightly varied (i.e., ranging from 5.0 to 5.4 ppm) for samples at different pH or when different saturation power were used (Figure 11c, d). As pH increased from 6.0 to 8.0, the MTR_{asym} value of CEST peak at 5.2 ppm increased as well.

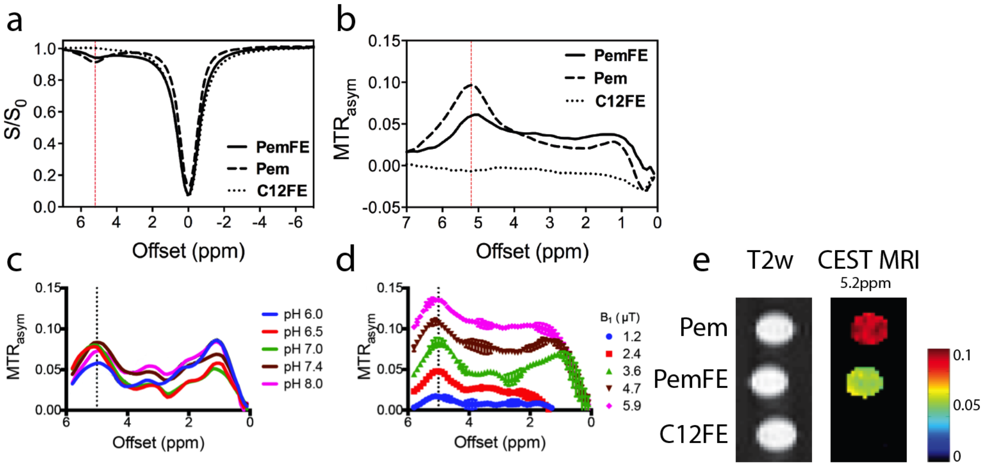

Figure 11. Basic CEST characterization. a) CEST spectra and b) MTRasym plot of **PemFE** (solid), **Pem** (dashed), and **C12FE** (dotted) showed CEST peaks at 5.2 ppm. The MTRasym plots of **PemFE** c) at different pH (using a B1=3.6μT), and d) acquired using different B1 values (pH=7.4). The vertical line shows the offset at 5.2 ppm. e) Color coded CEST contrast map of **Pem**, **PemFE**, and **C12FE** with respect to 5.2 ppm offset from water.

At the same concentration, **PemFE** showed slightly lower CEST signal compared to free **Pem**. We speculate that the self-assembly of **PemFE** into core-shell structure, which positioned **Pem** in the center of nanofiber structure is limiting the accessibility of **Pem**-exchanging proton to the surrounding water protons, therefore exhibited a slightly lower CEST signal than free **Pem** (Figure 11a, b). The suppression or acceleration of proton exchange rates, as a result of distinct water exposure of exchanging protons has been reported in other literature as well, to probe the differences in protein conformational structures[77, 78]. Nevertheless, **PemFE** is still CEST-detectable and its CEST signal at 5.2 ppm offset is markedly higher compared to the control molecule, **C12FE** (Figure 11a, b, e), which allows the direct detection of **PemFE** using CEST MRI.

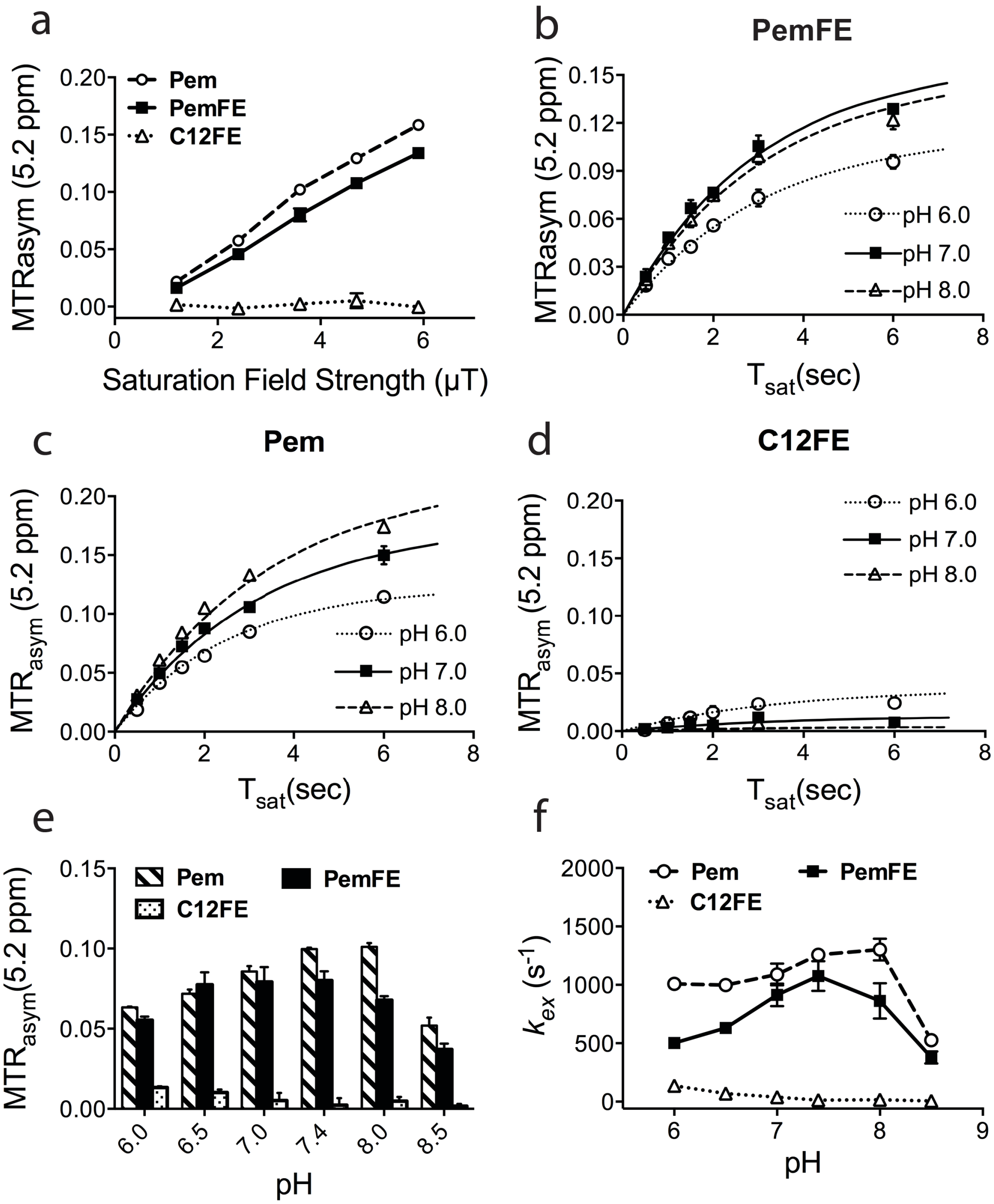

Figure 12. Comparing CEST properties of **PemFE**, **Pem** and **C12FE**, each at 10 mM in 1xDPBS solution at 37 °C. a) MTRasym at 5.2 ppm of all designed molecules at pH 7.4, measured at different saturation field strength; b) PemFE MTRasym at 5.2 ppm measured with respect to pre-saturation time (Tsat) at pH 6, 7, and 8. c) Pem MTRasym at 5.2 ppm measured with respect to pre-saturation time (Tsat) at pH 6, 7, and 8. d) C12FE MTRasym at 5.2 ppm measured with respect to pre-saturation time (Tsat) at pH 6, 7, and 8. e) MTRasym at 5.2 ppm as a function of pH using B1 = 3.6 μT. QUEST method was used to fit data and obtain kex values; f) pH dependence of proton exchange rate (kex) as a function of pH using B1 = 3.6 μT.

The apparent CEST effect is strongly dependent on the saturation parameters. Figure 12a shows that both **Pem** and **PemFE** (10 mM, pH 7.4) exhibited a linear increase with respect to higher saturation field strength (B_1). Considering higher B_1 also can cause a too strong direct water saturation effect and severe unwanted Magnetization Transfer effect for the *in vivo* cases, we chose B_1 = 3.6 μT for subsequent *in vivo* studies. Figure 12b showed the example of the QUEST analysis of saturation time (T_{sat})-dependent CEST effect of **PemFE** at pH 6 (dotted line), pH 7 (solid line), and pH 8 (dashed line). The same analysis was performed for **Pem** and **C12FE** and results are shown in Figure 12c, d. As expected, MTR_{asym} at 5.2ppm increased with increasing T_{sat} for Pem-containing molecules. However, for T_{sat} longer than 3 seconds, CEST effect did not increase significantly. Therefore, a T_{sat} of 3 seconds was considered as the optimal value and was used in the subsequent studies.

When studied in the pH range from pH 6.0 to pH 8.5, **Pem**, **PemFE** and **C12FE** exhibited different pH-dependence CEST contrast as shown in Figure 12e. Both free **Pem** and **PemFE** had a biphasic response, i.e., first increased and then decreased, to the pH increase. The maximal CEST contrasts were observed at pH 7.4 and pH 7.0 for **Pem** and **PemFE** respectively; **C12FE** clearly showed a continuously decrease of CEST contrast when pH increased although the maximal CEST contrast was only 0.01± 0.001. The high correlation of **Pem** and **PemFE** CEST contrast to pH condition indicated that the exchange rate (k_{sw}) of **Pem** amine proton changed dramatically at different pH. To estimate the exchange rate (k_{ex}), we measured the MTR_{asym} values at 5.2 ppm with saturation time (T_{sat}) ranging from 0.5 to 6 seconds and analyzed the data using the previously reported QUEST (QUantifying Exchange rates using Saturation Time) method[79]. The pH dependence of proton exchange rate (k_{ex}) of each compound is shown in Figure 12f. The estimated **Pem** proton exchange rate is in the order of 10^2-10^3 s^{-1}, which is comparable to k_{ex} reported in other literature.[45, 49] Both **Pem** and **PemFE** clearly exhibited a biphasic k_{ex} function with respect to pH (Figure 12f). The initial pH-dependent increase is attributed to the gradual increase of exchange rate when pH increases like all the base-catalyzed proton exchanges[77]. However, the second phase in which k_{ex} drops when pH further increases is unexpected. We speculate it is because the further increase of pH indeed makes the k_{ex} too fast that has exceeded the slow-to-moderate exchange rate region (i.e., $k_{ex} > \Delta\omega$), which instead compromises the CEST signal and lowers the apparent CEST contrast.

4.4 *In vivo* CEST MRI Time-Point Study and Spatial Comparison

In vivo study demonstrated that the injected **PemFE** hydrogel in mouse glioma tumors could be detected using CEST MRI for up to 4 days post-implantation. To assess the potential use of **PemFE** hydrogel *in vivo*, a GL261 orthotopic brain tumor model was used. In brief, C57BL6 mice (female, 5-6 weeks, n=5) were stereotactically injected with 2×10^4 GL261 cells in the right hemisphere of mouse brain. Twenty-five days after the inoculation of tumor cells, hydrogel was injected into the tumors using the same stereotactic settings and *in vivo* MRI was performed before and after 2 and 96 hours post-injection on a Biospec11.7 T MRI scanner equipped with a 23 mm mouse brain volume coil. CEST MRI acquisition and data processed were performed as previously reported (B_1= 3.6 μT and T_{sat}= 3 sec)[75]. As shown in Figure 13a, a localized but not uniform **PemFE** hydrogel distribution in the tumor could be appreciated by comparing the CEST MRI signal acquired at 2 hours after the injection and that before injection. After 4 days, **PemFE** hydrogel was still CEST detectable but appeared as a more uniform distribution in a larger area, indicating a slow gradient-driven diffusion to nearby tumor cells. This study clearly demonstrated that **PemFE** hydrogel is a promising slow-release implantable drug delivery system with its location and distribution directly monitored by CEST MRI without any imaging agents.

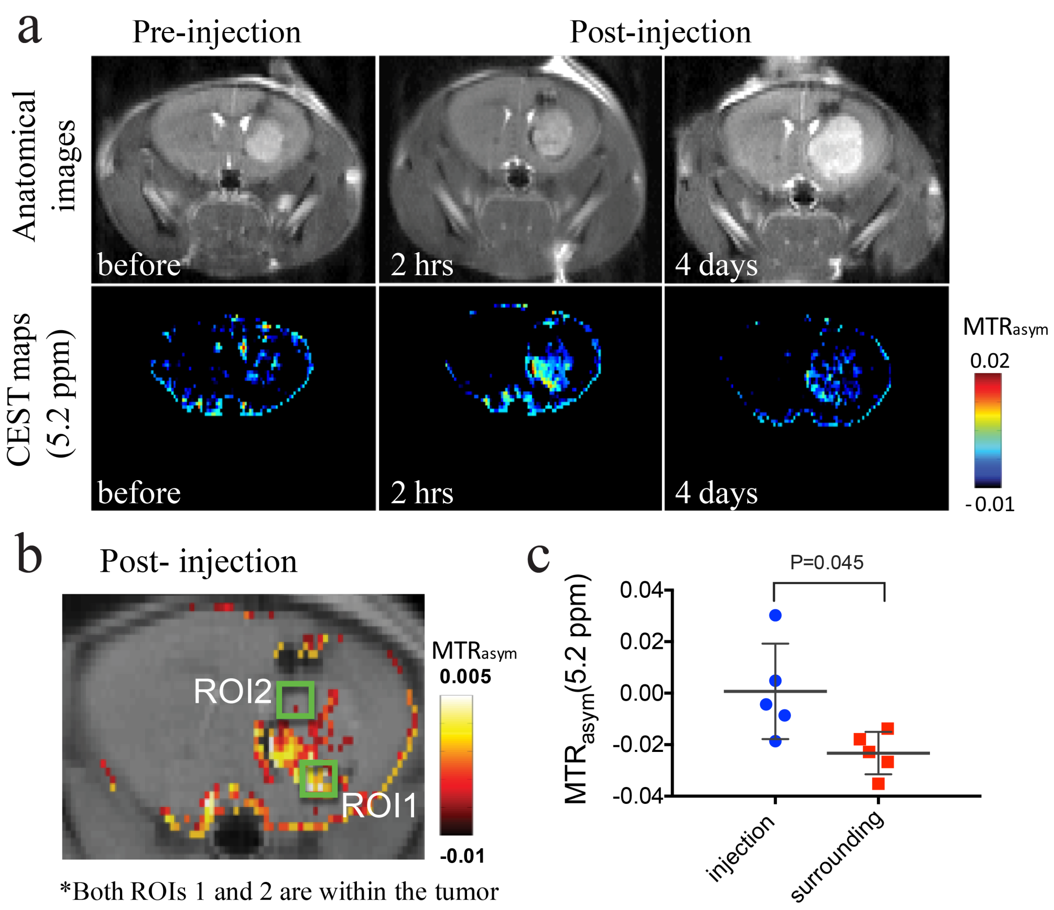

*Both ROIs 1 and 2 are within the tumor

Figure 13. MRI detection of **PemFE**, pemetrexed (Alimta) conjugated nanofibers hydrogel that was stereotactically injected in brain tumors (day 25 after tumor implantation). a) On the top, MRI images showing GL261 brain tumor at different time points (with respect to the time of injection of nanofiber hydrogel); On the bottom, CEST maps at 5.2 ppm of the mouse brain before, 2 hours and 4 days after the **PemFE** injection. b) Illustration of choosing ROIs on overlaid CEST images at 2 hours after the **PemFE** hydrogel injection to represent tumor regions of ROI1 - the **PemFE** injection site with increased CEST contrast and ROI2 - its surrounding region, without CEST contrast. c) The quantification of CEST contrast showing a significant higher MTRasym values for **PemFE** injection site than surrounding tumor ($P > 0.05$, two-tailed, paired Student t-test, $n=5$).

To further evaluate the imaging capability of **PemFE** hydrogel, we quantitatively analyzed the CEST MRI signal at the injection site compared to its surrounding/background. Figure 13b showed an overlay image of the CEST parametric map (threshold by $MTR_{asym} > -0.01$) at 2 hours post-injection of **PemFE** hydrogel and a T2w anatomical image. We chose two ROIs (region of interest - ROI) in the tumor with ROI1 representing the region has a strong signal and ROI2 representing the region that has low CEST MRI contrast. Then we repeated the same analysis on four more mice. As shown in Figure 13c, the mean CEST contrast between the ROI1 (injection site in the tumor) and ROI2 (surrounding region in the corresponding tumor) was 0.024 in MTR_{asym}, which is statistical significant (P=0.045, two-tailed, paired Student t-test).

Chapter 5: Conclusions

In summary, we successfully developed a novel CEST MRI detectable drug-peptide nanofiber hydrogel system. With the inherent CEST MRI signal carried by Pem-containing molecules at 5.2 ppm, the location, distribution and drug release of the injected **PemFE** hydrogel could be easily monitored by CEST MRI in a label-free manner. The conjugation of self-assembling peptide to **Pem** drug entails the formation of **PemFE** nanofibers hydrogel, exhibits slow-release characteristic of **Pem** over time. This new injectable and CEST MRI-detectable nanofiber hydrogel will be ideal for image-guided drug delivery of anticancer drug Pemetrexed (**Pem**) because it solely composed of the drug (**Pem**) and peptide (FFEE) and the MRI detectability stems from the inherent CEST signal of **Pem**. The proof-of-concept in using drug-peptide nanofiber for *in vivo* CEST MRI detection was demonstrated in an orthotopic brain tumor mouse model. While further therapeutic evaluations are anticipated, the current study demonstrated a strategy for constructing metal-free and highly translatable MRI guided drug-delivery system.

References

1. Mao X, Xu J, Cui H. Functional nanoparticles for magnetic resonance imaging. *Wiley Interdiscip Rev Nanomed Nanobiotechnol* 2016. doi: 10.1002/wnan.1400
2. Liu G, Song X, Chan KW, McMahon MT. Nuts and bolts of chemical exchange saturation transfer MRI. *NMR Biomed* 2013, 26:810-828. doi: 10.1002/nbm.2899
3. van Zijl PC, Yadav NN. Chemical exchange saturation transfer (CEST): what is in a name and what isn't? *Magn Reson Med* 2011, 65:927-948. doi: 10.1002/mrm.22761
4. Brown MA, Semelka RC. *MRI: Basic Principles and Applications*: Wiley, 2011.
5. Tang H, Wu EX, Ma QY, Gallagher D, Perera GM, Zhuang T. MRI brain image segmentation by multi-resolution edge detection and region selection. *Computerized Medical Imaging and Graphics* 2000, 24:349-357. doi: 10.1016/s0895-6111(00)00037-9
6. Sipkins DA, Cheresh DA, Kazemi MR, Nevin LM, Bednarski MD, Li KCP. Detection of tumor angiogenesis in vivo by αvβ3-targeted magnetic resonance imaging. *Nature Medicine* 1998, 4:623-626. doi: 10.1038/nm0598-623
7. Hung AH, Duch MC, Parigi G, Rotz MW, Manus LM, Mastarone DJ, Dam KT, Gits CC, Macrenaris KW, Luchinat C, et al. Mechanisms of Gadographene-Mediated Proton Spin Relaxation. *J Phys Chem C Nanomater Interfaces* 2013, 117. doi: 10.1021/jp406909b
8. Matosziuk LM, Leibowitz JH, Heffern MC, MacRenaris KW, Ratner MA, Meade TJ. Structural optimization of Zn(II)-activated magnetic resonance imaging probes. *Inorg Chem* 2013, 52:12250-12261. doi: 10.1021/ic400681j
9. Bulte JW, Kraitchman DL. Iron oxide MR contrast agents for molecular and cellular imaging. *NMR Biomed* 2004, 17:484-499. doi: 10.1002/nbm.924
10. Huang CH, Tsourkas A. Gd-based Macromolecules and Nanoparticles as Magnetic Resonance Contrast Agents for Molecular Imaging. *Current Topics in Medicinal Chemistry* 2013, 13:411-421
11. Tassa C, Duffner JL, Lewis TA, Weissleder R, Schreiber SL, Koehler AN, Shaw SY. Binding affinity and kinetic analysis of targeted small molecule-modified nanoparticles. *Bioconjug Chem* 2010, 21:14-19. doi: 10.1021/bc900438a
12. Janib SM, Moses AS, MacKay JA. Imaging and drug delivery using theranostic nanoparticles. *Adv Drug Deliv Rev* 2010, 62:1052-1063. doi: 10.1016/j.addr.2010.08.004
13. Bridot JL, Faure AC, Laurent S, Riviere C, Billotey C, Hiba B, Janier M, Josserand V, Coll JL, Elst LV, et al. Hybrid gadolinium oxide nanoparticles: multimodal contrast agents for in vivo imaging. *J Am Chem Soc* 2007, 129:5076-5084. doi: 10.1021/ja068356j
14. Wang AZ, Langer R, Farokhzad OC. Nanoparticle delivery of cancer drugs. *Annu Rev Med* 2012, 63:185-198. doi: 10.1146/annurev-med-040210-162544
15. Gao J, Xu B. Applications of nanomaterials inside cells. *Nano Today* 2009, 4:37-51. doi: 10.1016/j.nantod.2008.10.009
16. Zhou Z, Lu ZR. Gadolinium-based contrast agents for magnetic resonance cancer imaging. *Wiley Interdiscip Rev Nanomed Nanobiotechnol* 2013, 5:1-18. doi: 10.1002/wnan.1198
17. Konda SD, Aref M, Wang S, Brechbiel M, Wiener EC. Specific targeting of folate–dendrimer MRI contrast agents to the high affinity folate receptor expressed in ovarian tumor xenografts. *Magma: Magnetic Resonance Materials in Physics, Biology, and Medicine* 2001, 12:104-113. doi: 10.1007/bf02668091
18. Saito R, Krauze MT, Bringas JR, Noble C, McKnight TR, Jackson P, Wendland MF, Mamot C, Drummond DC, Kirpotin DB, et al. Gadolinium-loaded liposomes allow for real-time

magnetic resonance imaging of convection-enhanced delivery in the primate brain. *Exp Neurol* 2005, 196:381-389. doi: 10.1016/j.expneurol.2005.08.016

19. Mulder WJ, Koole R, Brandwijk RJ, Storm G, Chin PT, Strijkers GJ, de Mello Donega C, Nicolay K, Griffioen AW. Quantum dots with a paramagnetic coating as a bimodal molecular imaging probe. *Nano Lett* 2006, 6:1-6. doi: 10.1021/nl051935m
20. Taylor KM, Kim JS, Rieter WJ, An H, Lin W, Lin W. Mesoporous silica nanospheres as highly efficient MRI contrast agents. *J Am Chem Soc* 2008, 130:2154-2155. doi: 10.1021/ja710193c
21. Ananta JS, Godin B, Sethi R, Moriggi L, Liu X, Serda RE, Krishnamurthy R, Muthupillai R, Bolskar RD, Helm L, et al. Geometrical confinement of gadolinium-based contrast agents in nanoporous particles enhances T1 contrast. *Nat Nanotechnol* 2010, 5:815-821. doi: 10.1038/nnano.2010.203
22. Bull SR, Guler MO, Bras RE, Venkatasubramanian PN, Stupp SI, Meade TJ. Magnetic resonance imaging of self-assembled biomaterial scaffolds. *Bioconjug Chem* 2005, 16:1343-1348. doi: 10.1021/bc050153h
23. Webber MJ, Kessler JA, Stupp SI. Emerging peptide nanomedicine to regenerate tissues and organs. *J Intern Med* 2010, 267:71-88. doi: 10.1111/j.1365-2796.2009.02184.x
24. Ortony JH, Newcomb CJ, Matson JB, Palmer LC, Doan PE, Hoffman BM, Stupp SI. Internal dynamics of a supramolecular nanofibre. *Nat Mater* 2014, 13:812-816. doi: 10.1038/nmat3979
25. Nicolle GM, Toth E, Eisenwiener KP, Macke HR, Merbach AE. From monomers to micelles: investigation of the parameters influencing proton relaxivity. *J Biol Inorg Chem* 2002, 7:757-769. doi: 10.1007/s00775-002-0353-3
26. Bull SR, Guler MO, Bras RE, Meade TJ, Stupp SI. Self-assembled peptide amphiphile nanofibers conjugated to MRI contrast agents. *Nano Lett* 2005, 5:1-4. doi: 10.1021/nl0484898
27. Liu S, Zhang P, Banerjee SR, Xu J, Pomper MG, Cui H. Design and assembly of supramolecular dual-modality nanoprobes. *Nanoscale* 2015, 7:9462-9466. doi: 10.1039/c5nr01518a
28. Caravan P, Ellison JJ, McMurry TJ, Lauffer RB. Gadolinium(III) Chelates as MRI Contrast Agents: Structure, Dynamics, and Applications. *Chemical Reviews* 1999, 99:2293-2352. doi: 10.1021/cr980440x
29. Preslar AT, Parigi G, McClendon MT, Sefick SS, Moyer TJ, Haney CR, Waters EA, MacRenaris KW, Luchinat C, Stupp SI, et al. Gd(III)-labeled peptide nanofibers for reporting on biomaterial localization in vivo. *ACS Nano* 2014, 8:7325-7332. doi: 10.1021/nn502393u
30. Appel AA, Anastasio MA, Larson JC, Brey EM. Imaging challenges in biomaterials and tissue engineering. *Biomaterials* 2013, 34:6615-6630. doi: 10.1016/j.biomaterials.2013.05.033
31. Longmire M, Choyke PL, Kobayashi H. Clearance properties of nano-sized particles and molecules as imaging agents: considerations and caveats. *Nanomedicine (Lond)* 2008, 3:703-717. doi: 10.2217/17435889.3.5.703
32. Heldin CH, Rubin K, Pietras K, Ostman A. High interstitial fluid pressure - an obstacle in cancer therapy. *Nat Rev Cancer* 2004, 4:806-813. doi: 10.1038/nrc1456
33. Lammers T, Kiessling F, Hennink WE, Storm G. Nanotheranostics and image-guided drug delivery: current concepts and future directions. *Mol Pharm* 2010, 7:1899-1912. doi: 10.1021/mp100228v

34. Chakravarty R, Hong H, Cai W. Positron emission tomography image-guided drug delivery: current status and future perspectives. *Mol Pharm* 2014, 11:3777-3797. doi: 10.1021/mp500173s
35. Seymour LW, Ferry DR, Anderson D, Hesslewood S, Julyan PJ, Poyner R, Doran J, Young AM, Burtles S, Kerr DJ, et al. Hepatic drug targeting: phase I evaluation of polymer-bound doxorubicin. *J Clin Oncol* 2002, 20:1668-1676. doi: 10.1200/jco.20.6.1668
36. Langereis S, Geelen T, Grull H, Strijkers GJ, Nicolay K. Paramagnetic liposomes for molecular MRI and MRI-guided drug delivery. *NMR Biomed* 2013, 26:728-744. doi: 10.1002/nbm.2971
37. Bohmer MR, Klibanov AL, Tiemann K, Hall CS, Gruell H, Steinbach OC. Ultrasound triggered image-guided drug delivery. *Eur J Radiol* 2009, 70:242-253. doi: 10.1016/j.ejrad.2009.01.051
38. Grobner T. Gadolinium--a specific trigger for the development of nephrogenic fibrosing dermopathy and nephrogenic systemic fibrosis? *Nephrol Dial Transplant* 2006, 21:1104-1108. doi: 10.1093/ndt/gfk062
39. Kanda T, Fukusato T, Matsuda M, Toyoda K, Oba H, Kotoku J, Haruyama T, Kitajima K, Furui S. Gadolinium-based Contrast Agent Accumulates in the Brain Even in Subjects without Severe Renal Dysfunction: Evaluation of Autopsy Brain Specimens with Inductively Coupled Plasma Mass Spectroscopy. *Radiology* 2015, 276:228-232. doi: 10.1148/radiol.2015142690
40. Ward KM, Aletras AH, Balaban RS. A new class of contrast agents for MRI based on proton chemical exchange dependent saturation transfer (CEST). *Journal of Magnetic Resonance* 2000, 143:79-87. doi: DOI 10.1006/jmre.1999.1956
41. Liu GS, Song XL, Chan KWY, McMahon MT. Nuts and bolts of chemical exchange saturation transfer MRI. *Nmr in Biomedicine* 2013, 26:810-828. doi: 10.1002/nbm.2899
42. Liu GS, Liang YJ, Bar-Shir A, Chan KWY, Galpoththawela CS, Bernard SM, Tse T, Yadav NN, Walczak P, McMahon MT, et al. Monitoring Enzyme Activity Using a Diamagnetic Chemical Exchange Saturation Transfer Magnetic Resonance Imaging Contrast Agent. *Journal of the American Chemical Society* 2011, 133:16326-16329. doi: Doi 10.1021/Ja204701x
43. McVicar N, Li AX, Goncalves DF, Bellyou M, Meakin SO, Prado MAM, Bartha R. Quantitative tissue pH measurement during cerebral ischemia using amine and amide concentration-independent detection (AACID) with MRI. *Journal of Cerebral Blood Flow and Metabolism* 2014, 34:690-698. doi: 10.1038/jcbfm.2014.12
44. Zhou JY, Payen JF, Wilson DA, Traystman RJ, van Zijl PCM. Using the amide proton signals of intracellular proteins and peptides to detect pH effects in MRI. *Nature Medicine* 2003, 9:1085-1090. doi: Doi 10.1038/Nm907
45. Yang X, Song XL, Li YG, Liu GS, Banerjee SR, Pomper MG, McMahon MT. Salicylic Acid and Analogues as diaCEST MRI Contrast Agents with Highly Shifted Exchangeable Proton Frequencies. *Angewandte Chemie-International Edition* 2013, 52:8116-8119. doi: 10.1002/anie.201302764
46. Longo DL, Dastru W, Digilio G, Keupp J, Langereis S, Lanzardo S, Prestigio S, Steinbach O, Terreno E, Uggeri F, et al. Iopamidol as a Responsive MRI-Chemical Exchange Saturation Transfer Contrast Agent for pH Mapping of Kidneys: In Vivo Studies in Mice at 7 T. *Magnetic Resonance in Medicine* 2011, 65:202-211. doi: 10.1002/mrm.22608
47. Chen LQ, Howison CM, Jeffery JJ, Robey IF, Kuo PH, Pagel MD. Evaluations of Extracellular pH within In Vivo Tumors Using acidoCEST MRI. *Magnetic Resonance in Medicine* 2014, 72:1408-1417. doi: 10.1002/mrm.25053

48. Chen LQ, Randtke EA, Jones KM, Moon BF, Howison CM, Pagel MD. Evaluations of Tumor Acidosis Within In Vivo Tumor Models Using Parametric Maps Generated with AcidoCEST MRI. *Molecular Imaging and Biology* 2015, 17:488-496. doi: 10.1007/s11307-014-0816-2
49. Longo DL, Sun PZ, Consolino L, Michelotti FC, Uggeri F, Aime S. A General MRI-CEST Ratiometric Approach for pH Imaging: Demonstration of in Vivo pH Mapping with lobitridol. *Journal of the American Chemical Society* 2014, 136:14333-14336. doi: 10.1021/ja5059313
50. Li Y, Chen H, Xu J, Yadav NN, Chan KW, Luo L, McMahon MT, Vogelstein B, van Zijl PC, Zhou S, et al. CEST theranostics: label-free MR imaging of anticancer drugs. *Oncotarget* 2016. doi: 10.18632/oncotarget.7141
51. Snoussi K, Bulte JW, Guéron M, van Zijl P. Sensitive CEST agents based on nucleic acid imino proton exchange: Detection of poly (rU) and of a dendrimer ‐ poly (rU) model for nucleic acid delivery and pharmacology. *Magnetic Resonance in Medicine* 2003, 49:998-1005
52. Choi J, Kim K, Kim T, Liu G, Bar-Shir A, Hyeon T, McMahon MT, Bulte JW, Fisher JP, Gilad AA. Multimodal imaging of sustained drug release from 3-D poly (propylene fumarate)(PPF) scaffolds. *Journal of Controlled Release* 2011, 156:239-245
53. Song X, Airan RD, Arifin DR, Bar-Shir A, Kadayakkara DK, Liu G, Gilad AA, van Zijl PC, McMahon MT, Bulte JW. Label-free in vivo molecular imaging of underglycosylated mucin-1 expression in tumour cells. *Nature communications* 2015, 6
54. Dula AN, Arlinghaus LR, Dortch RD, Dewey BE, Whisenant JG, Ayers GD, Yankeelov TE, Smith SA. Amide proton transfer imaging of the breast at 3 T: establishing reproducibility and possible feasibility assessing chemotherapy response. *Magnetic Resonance in Medicine* 2013, 70:216-224
55. Sagiyama K, Mashimo T, Togao O, Vemireddy V, Hatanpaa KJ, Maher EA, Mickey BE, Pan E, Sherry AD, Bachoo RM. In vivo chemical exchange saturation transfer imaging allows early detection of a therapeutic response in glioblastoma. *Proceedings of the National Academy of Sciences* 2014, 111:4542-4547
56. Hazarika M, White RM, Johnson JR, Pazdur R. FDA drug approval summaries: Pemetrexed (Alimta (R)). *Oncologist* 2004, 9:482-488. doi: DOI 10.1634/theoncologist.9-5-482
57. Liu G, Gilad AA, Bulte JW, van Zijl PC, McMahon MT. High-throughput screening of chemical exchange saturation transfer MR contrast agents. *Contrast Media Mol Imaging* 2010, 5:162-170. doi: 10.1002/cmmi.383
58. Kim M, Gillen J, Landman BA, Zhou J, Zijl PCMv. Water saturation shift referencing (WASSR) for chemical exchange saturation transfer (CEST) experiments. *Magnetic Resonance in Medicine* 2009, 61:1441-1450
59. McMahon MT, Gilad AA, Zhou J, Sun PZ, Bulte JW, van Zijl PC. Quantifying exchange rates in chemical exchange saturation transfer agents using the saturation time and saturation power dependencies of the magnetization transfer effect on the magnetic resonance imaging signal (QUEST and QUESP): Ph calibration for poly-L-lysine and a starburst dendrimer. *Magnetic Resonance in Medicine* 2006, 55:836-847. doi: 10.1002/mrm.20818
60. Cheetham AG, Zhang P, Lin YA, Lock LL, Cui H. Supramolecular nanostructures formed by anticancer drug assembly. *Journal of the American Chemical Society* 2013, 135:2907-2910. doi: 10.1021/ja3115983

61. Lin R, Cheetham AG, Zhang P, Lin YA, Cui H. Supramolecular filaments containing a fixed 41% paclitaxel loading. *Chem Commun (Camb)* 2013, 49:4968-4970. doi: 10.1039/c3cc41896k
62. Lin YA, Cheetham AG, Zhang P, Ou YC, Li Y, Liu G, Hermida-Merino D, Hamley IW, Cui H. Multiwalled nanotubes formed by catanionic mixtures of drug amphiphiles. *Acs Nano* 2014, 8:12690-12700. doi: 10.1021/nn505688b
63. Lock LL, LaComb M, Schwarz K, Cheetham AG, Lin YA, Zhang P, Cui H. Self-assembly of natural and synthetic drug amphiphiles into discrete supramolecular nanostructures. *Faraday Discuss* 2013, 166:285-301
64. Cheetham AG, Zhang PC, Lin YA, Lock LL, Cui HG. Supramolecular Nanostructures Formed by Anticancer Drug Assembly. *Journal of the American Chemical Society* 2013, 135:2907-2910. doi: Doi 10.1021/Ja3115983
65. Lin R, Cheetham AG, Zhang PC, Lin YA, Cui HG. Supramolecular filaments containing a fixed 41% paclitaxel loading. *Chemical Communications* 2013, 49:4968-4970. doi: Doi 10.1039/C3cc41896k
66. Frohlich E. The role of surface charge in cellular uptake and cytotoxicity of medical nanoparticles. *International Journal of Nanomedicine* 2012, 7:5577-5591. doi: Doi 10.2147/Ijn.S36111
67. Gazit E. A possible role for pi-stacking in the self-assembly of amyloid fibrils. *Faseb Journal* 2002, 16:77-83. doi: DOI 10.1096/fj.01-0442hyp
68. Guo C, Luo Y, Zhou RH, Wei GH. Probing the Self-Assembly Mechanism of Diphenylalanine-Based Peptide Nanovesicles and Nanotubes. *Acs Nano* 2012, 6:3907-3918. doi: Doi 10.1021/Nn300015g
69. Lin YA, Cheetham AG, Zhang PC, Ou YC, Li YG, Liu GS, Hermida-Merino D, Hamley IW, Cui HG. Multiwalled Nanotubes Formed by Catanionic Mixtures of Drug Amphiphiles. *Acs Nano* 2014, 8:12690-12700. doi: 10.1021/nn505688b
70. Duncan R. Polymer conjugates as anticancer nanomedicines. *Nature Reviews Cancer* 2006, 6:688-701. doi: Doi 10.1038/Nrc1958
71. Koutsopoulos S, Unsworth LD, Nagai Y, Zhang SG. Controlled release of functional proteins through designer self-assembling peptide nanofiber hydrogel scaffold. *Proceedings of the National Academy of Sciences of the United States of America* 2009, 106:4623-4628. doi: 10.1073/pnas.0807506106
72. Liang GL, Yang ZM, Zhang RJ, Li LH, Fan YJ, Kuang Y, Gao Y, Wang T, Lu WW, Xu B. Supramolecular Hydrogel of a D-Amino Acid Dipeptide for Controlled Drug Release in Vivo. *Langmuir* 2009, 25:8419-8422. doi: 10.1021/la804271d
73. Webber MJ, Matson JB, Tamboli VK, Stupp SI. Controlled release of dexamethasone from peptide nanofiber gels to modulate inflammatory response. *Biomaterials* 2012, 33:6823-6832. doi: 10.1016/j.biomaterials.2012.06.003
74. Yan C, Altunbas A, Yucel T, Nagarkar RP, Schneider JP, Pochan DJ. Injectable solid hydrogel: mechanism of shear-thinning and immediate recovery of injectable beta-hairpin peptide hydrogels. *Soft Matter* 2010, 6:5143-5156. doi: 10.1039/C0SM00642D
75. Liu G, Moake M, Har-el YE, Long CM, Chan KW, Cardona A, Jamil M, Walczak P, Gilad AA, Sgouros G, et al. In vivo multicolor molecular MR imaging using diamagnetic chemical exchange saturation transfer liposomes. *Magnetic Resonance in Medicine* 2012, 67:1106-1113. doi: 10.1002/mrm.23100
76. Michalak O, Gruza MM, Witkowska A, Bujak I, Cmoch P. Synthesis and Physicochemical Characterization of the Impurities of Pemetrexed Disodium, an Anticancer Drug. *Molecules* 2015, 20:10004-10031. doi: 10.3390/molecules200610004

77. Liepinsh E, Otting G. Proton exchange rates from amino acid side chains - Implications for image contrast. *Magnetic Resonance in Medicine* 1996, 35:30-42. doi: DOI 10.1002/mrm.1910350106
78. Berndt KD, Beunink J, Schroder W, Wuthrich K. Designed Replacement of an Internal Hydration Water Molecule in Bpti - Structural and Functional Implications of a Glycine-to-Serine Mutation. *Biochemistry* 1993, 32:4564-4570. doi: DOI 10.1021/bi00068a012
79. McMahon MT, Gilad AA, Zhou JY, Sun PZ, Bulte JWM, van Zijl PCM. Quantifying exchange rates in chemical exchange saturation transfer agents using the saturation time and saturation power dependencies of the magnetization transfer effect on the magnetic resonance imaging signal (QUEST and QUESP): pH calibration for poly-L-lysine and a starburst dendrimer. *Magnetic Resonance in Medicine* 2006, 55:836-847. doi: 10.1002/mrm.20818

Curriculum Vitae

Xinpei Mao

2819 Damascus Ct, Apt E, Baltimore, MD, 21209, U.S.A.

(614) 632-2619, E-mail: xmao6@jhu.edu

EDUCATION

M.S.

Aug. 2014 – May. 2016 Johns Hopkins University, Baltimore, MD
Department of Chemical & Biomolecular Engineering
Advisor: Professor Honggang Cui

B.S.

Jan. 2012 – Aug. 2014 Ohio State University, Columbus, OH
Department of Chemical & Biomolecular Engineering

Sep. 2009 – Dec. 2011 Beijing Institute of Technology, Beijing, China
Department of Chemical Engineering

HONORS/AWARDS

2015	Acta Biomaterialia Poster Award, 2nd International Conference on Bioinspired and Zwitterionic Materials (ICBZM), University of Washington, Seattle, WA.
2013-2014	The George S. Bonn Scholarship, Ohio State University
2012-2013	Dean's List of four semesters, Ohio State University
2011	Excellent Student Award, Beijing Institute of technology
2009-2011	Department Scholarship, Beijing Institute of technology

PUBLICATION

1. Mao, X., Xu, J., Cui, H., "Functional Nanoparticles for Magnetic Resonance Imaging", ***WIRES Nanomedicine and Nanobiotechnology***, 2016. DOI: 10.1002/wnan.1400
2. Lock, L.L., Li, Y., Mao, X., Chen, H., Staedtke, V., and Bai, R., Liu G., and Cui, H., "Label-Free CEST MRI Detection of Self-Assembling Drug-Peptide Nanofiber Hydrogel", manuscript in preparation.

RESEARCH EXPERIENCE

1. Dec. 2014 – Present Prof. Honggang Cui Research Group, Johns Hopkins University

a) Peptide-based nanostructures as MRI contrast agents
-Designed and synthesized self-assembling peptide amphiphiles
-Studied the effect of the number and location of arginine residues on the morphology of their self-assembled nanostructures as well as on their MRI signals.
b) MRI-Trackable Self-Assembling Drug-Peptide Nanofiber Hydrogel (collaborative project)
-Image-guided drug delivery of anticancer drug Pemetrexed
-Responsible for drug-peptide synthesis, purification, characterization (Mass Spectrometry, TEM, CD, Hydrogel Release Rate, Cytotoxicity, Cell Culture), and CEST sample preparation

2. Feb. 2013 – Aug. 2013 Prof. Liang-Shih Fan Research Group, Ohio State University

Formation Mechanisms of Micro-Sized Core-Shell Particles via Cyclic Gas-Solid Reactions
-Designed Protocol to prepare micro-sized particles
-Operated TGA, XRD and BET for synthesis and sample property analysis

3. Sep. 2013- Jan. 2014 Senior Project, Ohio State University
Polymer Foam Extrusion
-Determined how polymer composition (blend of polystyrene and polypropylene) and operating parameters would affect the morphology and rheology of the polymer foam

LEADERSHIP

2015 Mentored 4 researchers
-2 junior undergraduate students from Chemical & Biomolecular Engineering department, Johns Hopkins University
-1 senior undergraduate student through the Research Experience for Undergrads (REU) Program
-1 high school student through the Women in Science and Engineering (WISE) program

Skills

-Technical experience: Peptide Synthesis, HPLC, TEM, Cell Culture, MALDI-TOF, ESI-MS, CD, NMR, Confocal Microscopy, XRD, TGA, BET
-Software: Proficient skills in Microsoft Office, Photoshop, Illustrator, Prism for data analysis, Cartoon drawing, and Layout arrangement